Normal and Differential SAR Interferometry

Wolfgang Keydel
Microwaves and Radar Institute
German Aerospace Research Centre (DLR), Oberpfaffenhofen
Contact Address:
Mittelfeld 4, D-82229 Hechendorf, Germany
E-mail: wolfgang.keydel@dlr.de

Abstract

SAR Interferometry explores the height structure inside a Radar pixel. Two antennas separated with a so called baseline distance B in cross velocity direction take two independent images from the same scene and compare the two phases which result from the same pixel at the two antennas. This phase differences compare to different distances between the pixel and the two antennas and from this difference the height of the respective pixel in relation to the altitude of the radar over a defined level can be determined.

The Interferogramme formation will be explained and the respective terminology will be presented. In this context basic relations and important geometrical and electrodynamics system parameters will be presented and defined, the phase unwrapping will be considered as well as basic interferometry processing procedures and image formation principles. Coherence is the basis for Interferometry as well as a careful calibration. Therefore, the role of interferometric coherence for image interpretation will be shown. Errors caused by phase noise, de-correlation, co-registration misalignment, atmospheric disturbances, baseline limits, etc will be considered. They, principally, are the main reasons for coherence degradation. Different Interferometry modes Cross Track and Along Track Interferometry, single and dual pass Interferometry, Differential Interferometry, and Permanent Scattering Interferometry SAR will be discussed.

1. Introduction

Goal of this lecture is to present the basics of SAR Interferometry in order to prepare the bottom for the following lectures on Polarimetric Interferometry and its applications. An Electromagnetic Field is characterized by Amplitude E_0, Frequency f, Phase φ and Polarization p, the latter describes the Vector character of the field $\underline{\epsilon}=(E_X;E_Y)$ principally as functions of time t. E_X and E_Y are orthogonal to each other and characterize the polarization base of a Transversal Electromagnetic wave (TEM wave) which has no component in propagation direction. It is sufficient for a principal understanding to consider in a first step "scalar" Electromagnetic Waves and there behavior. Tat means without limitation of generality one component of the Electric Field Vector only will be used, and polarization effects, principally, will be excluded. The scalar Electromagnetic Wave is written as:

$$E = E_0 \exp(i(2\pi f + \varphi)) \tag{1}$$

2. SAR Interferometry Principles

SAR Interferometry is an established technique for rapid and accurate collection of topographic data, which is essential for establishing Digital Elevation Models (DEM's), it allows the vertical location of the effective scattering centre inside the two dimensional horizontally oriented resolution cell.

Normally, SAR Interferometry works with two antennas separated in cross velocity direction characterized with the baseline distance B taking two independent images from the scene observed and comparing the two phases which result from the same pixel. This offers the capability to generate topographic maps. Adding a third flight at the same passes as before and subtracting the two results from each other is called Differential Interferometry.

Due to the distance between the antennas the distance to a single point scatterer on the ground is slightly different by the amount of *r*. This slant range difference *r* corresponds to a phase difference Φ comparing the received signals of both antennas. After detection of Φ the local terrain elevation above a well known reference area, a geoid for instance, can be determined according to the following equations, which are based on the geometry for SAR Interferometry depicted in Fig.1.

Keydel, W. (2007) Normal and Differential SAR Interferometry. In *Radar Polarimetry and Interferometry* (pp. 2-1 – 2-40). Educational Notes RTO-EN-SET-081bis, Paper 2. Neuilly-sur-Seine, France: RTO. Available from: http://www.rto.nato.int/abstracts.asp.

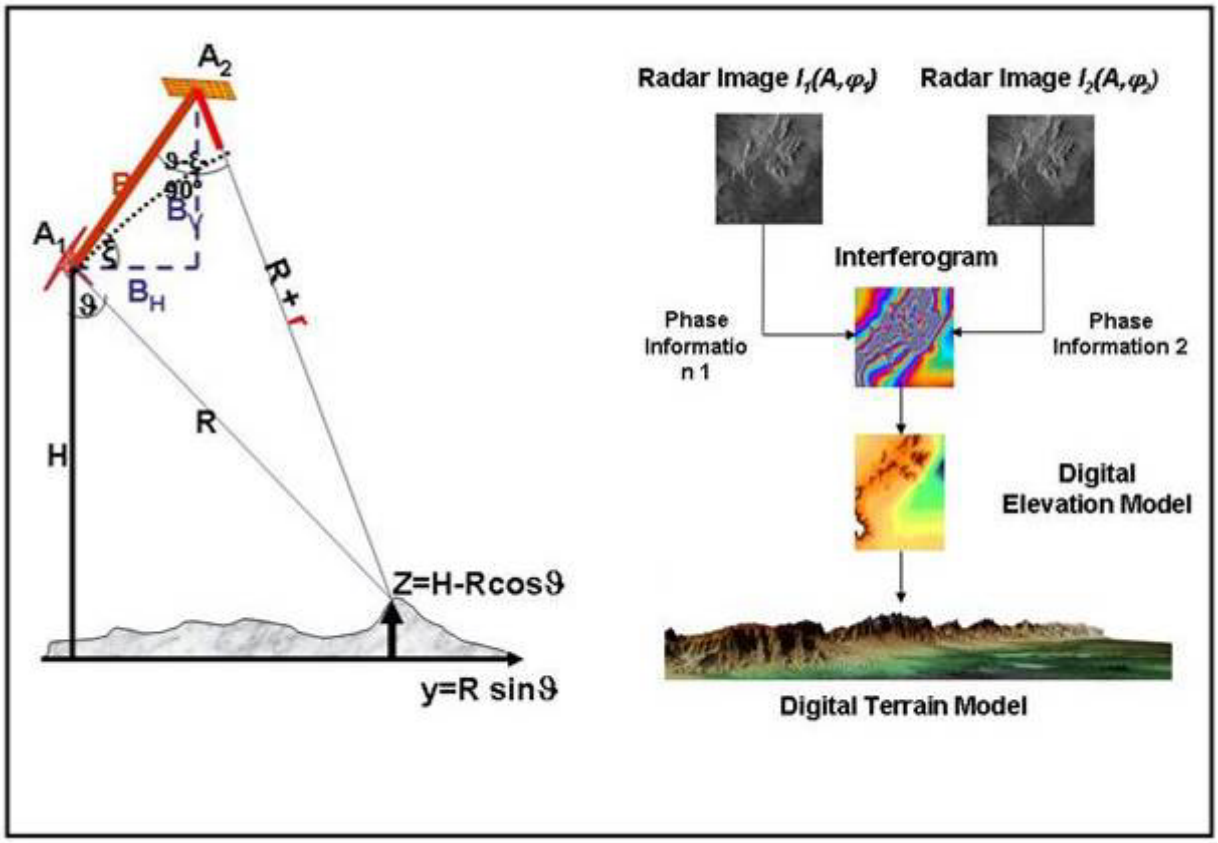

Fig.1 SAR Interferometry Principle

In practice two different methods are applied to obtain an interferometric baseline:

• **One pass Interferometry**: In this case both antennas are mounted rigidly to the same platform with a fixed baseline. There is one transmitter for the two receiving channels. An interferometric image is obtained after one pass of the platform. For the Phase difference results from the two phases φ_1 and φ_2:

$$\varphi_1 = 4\pi\frac{R_1}{\lambda}\ ,\ \varphi_2 = 2\pi\frac{2R_1 + r}{\lambda}$$

$$\Phi_{1\,pass} = \varphi_2 - \varphi_1 = 2\pi\frac{r}{\lambda}$$

• **Two pass Interferometry**: Only one Transmit-Receive channel with one antenna is used, but the platform has to pass the same terrain twice in the same direction along a trajectory parallel to the first one. In this case results for the Phases:

$$\varphi_1 = 4\pi\frac{R}{\lambda}\ ,\ \varphi_2 = 4\pi\frac{R+r}{\lambda}$$

$$\Phi_{2\,Pass} = \varphi_2 - \varphi_1 = 4\pi\frac{r}{\lambda}$$

For the Phase difference Φ_m will be written in the following:

$$\Phi_m = m\,2\pi\frac{r}{\lambda} \qquad (2)$$

With m=1 for the one pass case and m=2 for the two pass case. The propagation path difference 2*r* is usually much grater than the wave length, therefore,Φ normally shows an ambiguity of many cycles. In any case it can be determined mod 2π only, the phase is wrapped.

For topography purposes an across-track arrangement of the two sensors is essential. However, along track arrangements, principally, allow the measurements of the ground velocity if targets ore pixels respectively move between the two different imaging times between the two channels. Both modes are depicted in Fig. 2. The coherence between the two signals is essential in any case.

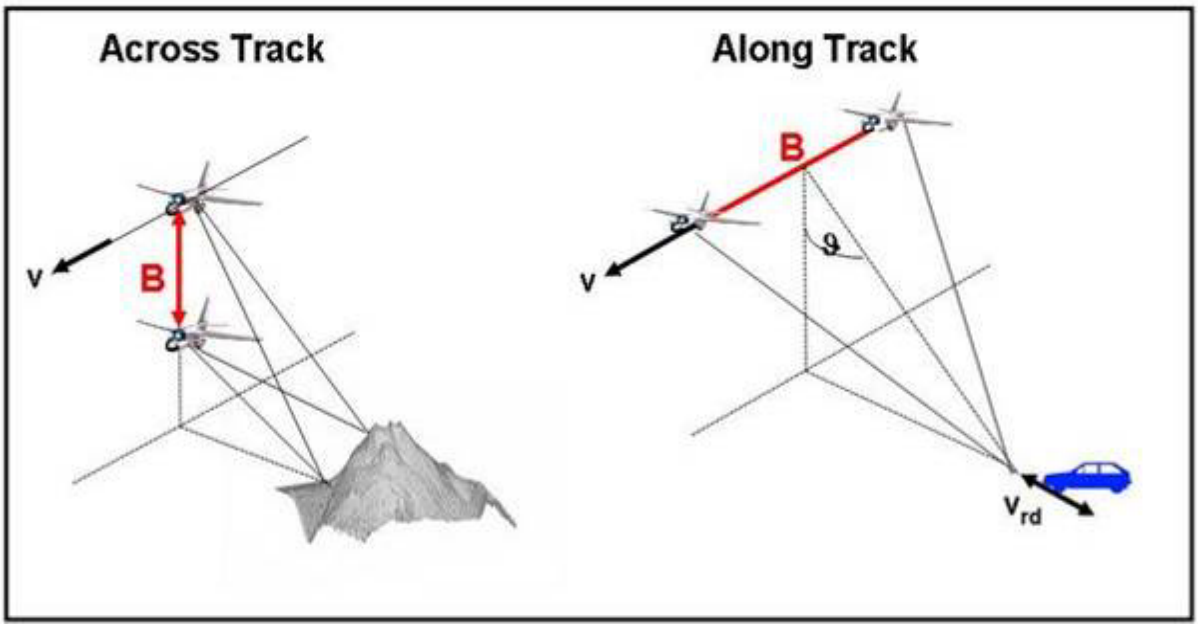

Fig. 2 Geometry of Across - and Along –Track SAR Interferometry Modes

2.1 Basic Interferogramme Relations

From the geometry depicted in Fig. 1 the following basic Interferometry relations result:

$$z = H - R\cos\vartheta \tag{3}$$

After some manipulations results for the slant range:

$$R = \frac{r^2 - B^2}{2B\sin(\vartheta - \xi) - 2r} \tag{4}$$

The imaging Geometry is given by

$$\sin(\vartheta - \xi) = \frac{r^2 - B^2}{2BR} + \frac{r}{B} \tag{5}$$

The ground range is determined by

$$y = R\sin\vartheta \tag{6}$$

The local terrain height z above the reference area is therefore:

$$z = H - \frac{r^2 - B^2}{2B\sin(\vartheta - \xi) - 2r}\cos\vartheta \tag{7}$$

In connection with (2) equation (7) delivers the desired Interferogramme as function of the look angle ϑ. In connection with (6) equation (7) delivers the ground range representation. The propagation path difference r for the both signals at the two antennas is:

$$r = m\left[\sqrt{R^2 + B^2 - 2BR\sin(\vartheta - \xi)} - R\right] \tag{8}$$

m=1for one pass Interferometry, m=2 for two pass interferometry with separate parallel flight passes. The corresponding phase difference Φ is:

$$\Phi = m\,2\pi\frac{r}{\lambda} = \frac{m\,2\pi}{\lambda}\left[\sqrt{R^2 + B^2 - 2BR\sin(\vartheta - \xi)} - R\right] \tag{9}$$

With equations (3) to (9) the topographic height z at each point on the y-axes can be determined as well as all the interrelations between all parameters for one Pixel.

The Interferogramme for the whole scene is generated by multiplying pixel by pixel the image I^*_1 with the complex conjugated image I^*_2 of the other. Unfortunately, the phase is represented as modulo 2π only, the phase is wrapped. Thus a "phase unwrapping" has to be carried out to obtain the absolute phase, which finally can be transformed to the desired height z at each point over the x-y-area leading to a three dimensional terrain elevation model.

For simplification it will be assumed B<<R which is realistic for the most airborne and all space-borne SAR systems used up to now. Under that condition results from a Taylor development of (9)

$$\Phi \approx m\frac{2\pi}{\lambda}\left[\frac{B^2}{2R} - B\sin(\vartheta - \xi)\right] \tag{10}$$

For both space-borne and the most airborne SAR the first term can be neglected also because

$$\frac{B^2}{2R} << B\sin(\vartheta - \xi)$$

For the most operational SAR Systems results:

$$\Phi \approx -m\frac{2\pi}{\lambda}B\sin(\vartheta - \xi) = -m\frac{2\pi}{\lambda}B_{par} \tag{11}$$

In (11) the factor $B_{par} = B\sin(\vartheta - \xi)$ is the Baseline component parallel to the look direction.

2.2 Interferometric Performance, Sensitivities and Errors.

All equations content both Radar System parameter and Interferometry parameter. For basic considerations the following Radar System parameter, principally, are assumed to be known a priori: The height H above a reference area (a special Geoid ore a flat area respectively), the baseline B, the wavelength λ used, the platform attitude represented by the baseline tilt angle ξ, the look angle ϑ, and the slant range distance R between the pixel observed at P_0, the both antennas A_1 *and* A_2 and the systems Phase Noise.

However, in reality all these parameters have to be determined by measurements during the flight and, therefore, errors will be introduced due to unavoidable measurement inaccuracies. That will be demonstrated exemplary for the dependency of the elevation variation Δz from the height variation ΔH. Principally holds under the assumption of small pixels for the variation of z as a function of the variation ΔH of H:

$$\frac{\Delta z}{\Delta H} \approx \frac{\partial z}{\partial H} \quad \Rightarrow \quad \Delta z \approx \frac{\partial z}{\partial H}\Delta H \tag{12}$$

The exemplary starting equation is (7) which gives the elevation z of the point P in Fig.2. In connection with (7) results for the elevation sensitivity Δz:

$$\Delta z = \Delta H \tag{13}$$

From the sensitivity Δz the quadratic error σ_z results in that case:

$$\sigma_z^2 = \left(\frac{\partial z}{\partial H}\right)^2 \sigma_H^2$$

The entire elevation measurement accuracy depends on the accuracy of the determination of both all the Radar System parameters and all the Interferometry parameters.

The general expression for the elevation errors is derived by adding the all quadratic errors:

$$\sigma_z^2 = \left[\frac{\partial z}{\partial H}\right]^2 \sigma_H^2 + \left[\frac{\partial z}{\partial R}\right]^2 \sigma_R^2 + \left[\frac{\partial z}{\partial \xi}\right]^2 \sigma_\xi^2 + \left[\frac{\partial z}{\partial \lambda}\right]^2 \sigma_\lambda^2 + \left[\frac{\partial z}{\partial \Phi}\right]^2 \sigma_\Phi^2 + \left[\frac{\partial z}{\partial B}\right]^2 \sigma_B^2 \tag{14}$$

The subscripts in (14) determine the respective Interferometry parameter.

Special interest has to be addressed to the 5th term, the Phase error σ_Φ. The total phase results from the sum of several contributions. The designations are self explaining:

$$\Phi = \Phi_{flatearth} + \Phi_{topography} + \Phi_{atmosphere} + \Phi_{motion} + \Phi_{noise} + \Phi_{Decorrelation} \tag{15}$$

The Phase errors Φ_{motion} caused by uncontrolled platform motions during the flight will be discussed more detailed in the Systems Lecture.

The sensitivity of a function Φ = Φ (z,y) against variations Δz and Δy respectively results from differentiation of the appropriate equations and can be expressed by the total Differential

$$d\Phi(z,y) = \frac{\partial \Phi}{\partial z} dz + \frac{\partial \Phi}{\partial y} dy \tag{16}$$

By replacing the symbol d with Δ and using the equations (7), (9), and (12) results:

$$\Delta\Phi = \frac{\partial \Phi}{\partial z}\Delta z + \frac{\partial \Phi}{\partial y}\Delta y \quad \text{with} \quad \frac{\partial \Phi}{\partial z} = \frac{\partial \Phi}{\partial \vartheta}\frac{\partial \vartheta}{\partial z} \quad \text{and} \quad \frac{\partial \Phi}{\partial y} = \frac{\partial \Phi}{\partial \vartheta}\frac{\partial \vartheta}{\partial y}$$

From (11) follows:

$$\frac{\partial \Phi}{\partial \vartheta} = -m\frac{2\pi}{\lambda} B\cos(\vartheta - \xi) = -m\frac{2\pi}{\lambda} B_{eff}$$

The factor B cos(ϑ-ξ) is called the effective Baseline B_{eff} vertical to the looking direction.

$$B_{eff} = B\cos(\vartheta - \xi) \tag{17}$$

With (6) follows both:

$$\frac{\partial \vartheta}{\partial z} = \frac{1}{R\sin\vartheta} \quad \text{and} \quad \frac{\partial \vartheta}{\partial y} = \frac{1}{R\cos\vartheta} \tag{18a) and (18b)}$$

Therefore, for the total phase variation in z- and y-direction results:

$$\Delta\Phi = -m\frac{2\pi}{\lambda}\frac{B}{R}\frac{\cos(\vartheta-\xi)}{\sin\vartheta}\Delta z - m\frac{2\pi}{\lambda}\frac{B}{R}\frac{\cos(\vartheta-\xi)}{\cos\vartheta}\Delta y \text{ with } -\pi \le \Phi \le +\pi \bmod 2\pi \tag{19}$$

This equation, principally, answers the question: Which Phase variation ΔΦ will be caused through terrain variations Δz in vertical ore Δy in horizontal direction? It delivers the interconnection between the measured phases and the height characteristics of the observed pixel. The first term represents the phase sensitivity against elevation variations in z-direction, the second term represents the sensitivity against a horizontal shift in a constant altitude z in y-direction taking into account the relations (3) and (6) again. Both terms represent interference patterns.

The second term is caused from the change in slant range observation distance R over the whole swath causing a fringe pattern parallel to the flight direction also. Equation (19) shows: the flat earth alone always causes a fringe pattern which overlays the topographic fringes additionally and, in order to observe and to analyze the topographic fringes only these two effects have to be separated by subtraction of the flat earth interferogram from the total observed interferometric phase (19).

The flat earth pattern is always present within the measurements because both R and (R + r) increase with increasing incidence angle, and B_{eff}, principally, changes its value also. The flat earth pattern has to be removed in order to obtain the pure elevation above the reference area which in this case is the flat area at z=0.

$$\Delta\Phi_z = -m\frac{2\pi}{\lambda}\frac{B_{eff}}{R\sin\vartheta}\Delta z = -m\frac{2\pi}{\lambda}B_{eff}\Delta\vartheta_{vert} \tag{20}$$

$$\Delta\Phi_{flat} = -m\frac{2\pi}{\lambda}\frac{B_{eff}}{R\cos\vartheta}\Delta y = -m\frac{2\pi}{\lambda}B_{eff}\Delta\vartheta_{hor} \tag{21}$$

The relation (20) delivers the required interference pattern between the measured phases and the terrain elevation z, i.e. a vertical shift of the observed point P, the relation (21) delivers the interference pattern which results from a horizontal shift of the observed pixel. $\Delta\vartheta_{vert}$ and $\Delta\vartheta_{hor}$ are the small looking angle variations for the horizontal and the vertical shifts of the point P respectively. From the geometry depicted in Fig.3 the following relations for $\Delta\vartheta_{vert}$ and $\Delta\vartheta_{hor}$ can be determined:

For the horizontal shift:

$$R\Delta\vartheta_{hor} \approx R\sin(\Delta\vartheta_{hor}) = \frac{\Delta R}{\tan\vartheta} \tag{22}$$

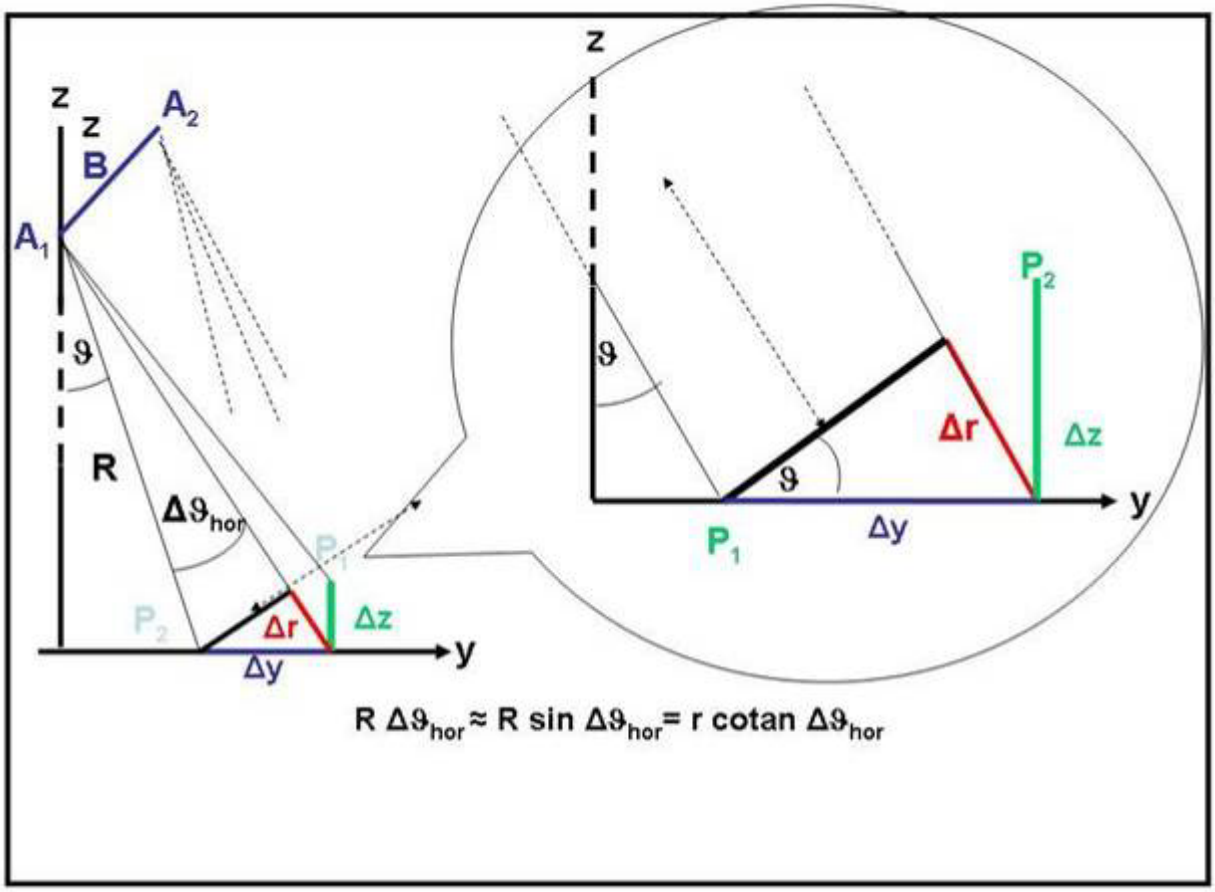

Fig.3 Demonstration of Geometry variation at small incidence angles

For the vertical shift:

$$R\Delta\vartheta_{vert} \approx R\sin(\Delta\vartheta_{vert}) = \frac{\Delta z}{\tan\vartheta} \tag{23}$$

Here with result from (19) and (20) the phase sensitivities for elevation and slant range variations.

$$\Delta\Phi_{flat} = -m\frac{2\pi}{\lambda}\frac{B_{eff}}{R\tan\vartheta}\Delta R \tag{24}$$

$$\Delta\Phi_{z} = -m\frac{2\pi}{\lambda}\frac{B_{eff}}{R\sin\vartheta}\Delta z \qquad -\pi \leq \Phi \leq \pi \tag{25}$$

The equations (21) and (24) represent the Interferogramme of the flat earth, i.e. an Interferogramme in absence of any topographic changes. The equations (20) and (25) represent the so called "flattened topographic Interferogramme" of the observed area in slant range representation. Both Interferogrammes have to be transformed into ground range presentations in order to obtain the desired results. The interconnection between ground range R_g and slant range R is:

$$R_g = R\sin\vartheta$$

With that relation results for the both Interferogrammes:

$$\Delta\Phi_{flat} = -m\frac{2\pi}{\lambda}B_{eff}\frac{\Delta R}{R}\cos\vartheta_g \tag{26}$$

$$\Delta\Phi_z = -m\frac{2\pi}{\lambda}\mathrm{B}_{\mathrm{eff}}\frac{\Delta z}{R_g} \tag{27}$$

In all equations varies **Φ mod 2π between -π and +π,** whilst **ΔΦ varies between -π and +π only**. The width of the fringes, principally, is given for $\Delta\Phi = 2\pi$. The sensitivity depends on the minimum phase measurement capability $\Delta\Phi_{min}$ of the sensor. The state of the art is $\mathbf{\Delta\Phi_{min} \approx 5°}$ which roughly corresponds to 1/70 of a wavelength. Fig.4 shows simply modeled fringe patterns of a cone; in Fig. 5 a real measurement result obtained from a hill formed like a cone is depicted, in the Figures 6, and 7 for a space-borne and an airborne case measured Interferogrammes over partially relative flat areas are depicted.

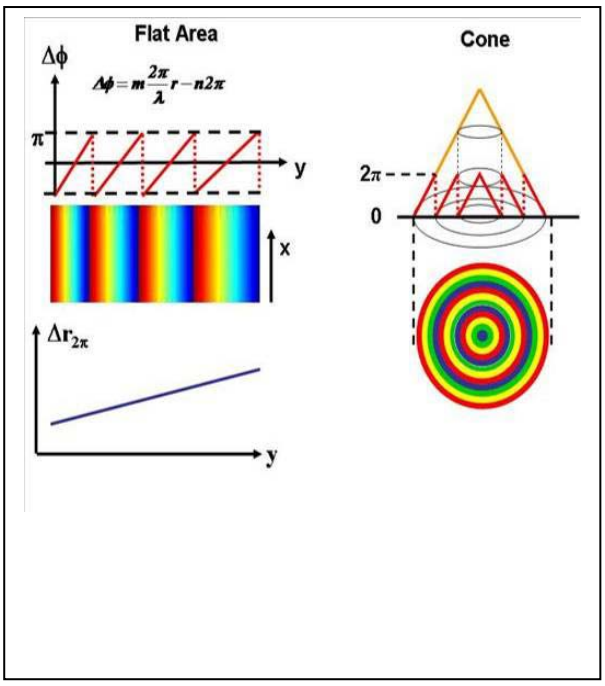

Fig.4 Models of fringe patterns for a flat area (left) and a modelled cone (right)

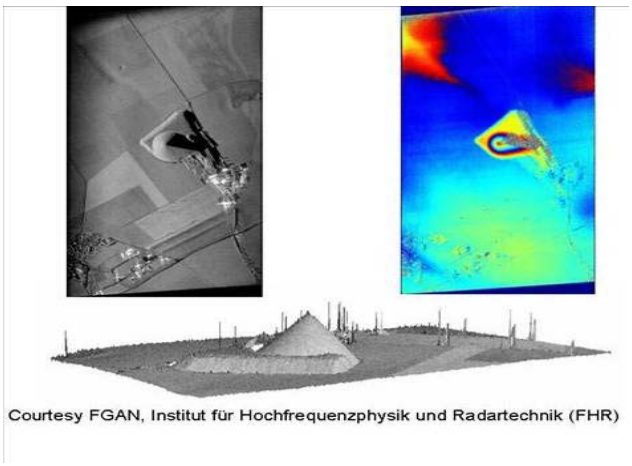

Fig.5 Measurement results over a flat area with a refuse Cone, amplitude (top left), phase fringes (top right), DEM below. The shadowing effect in the SAR image causing a complete loss of coherence is evident in the amplitude image

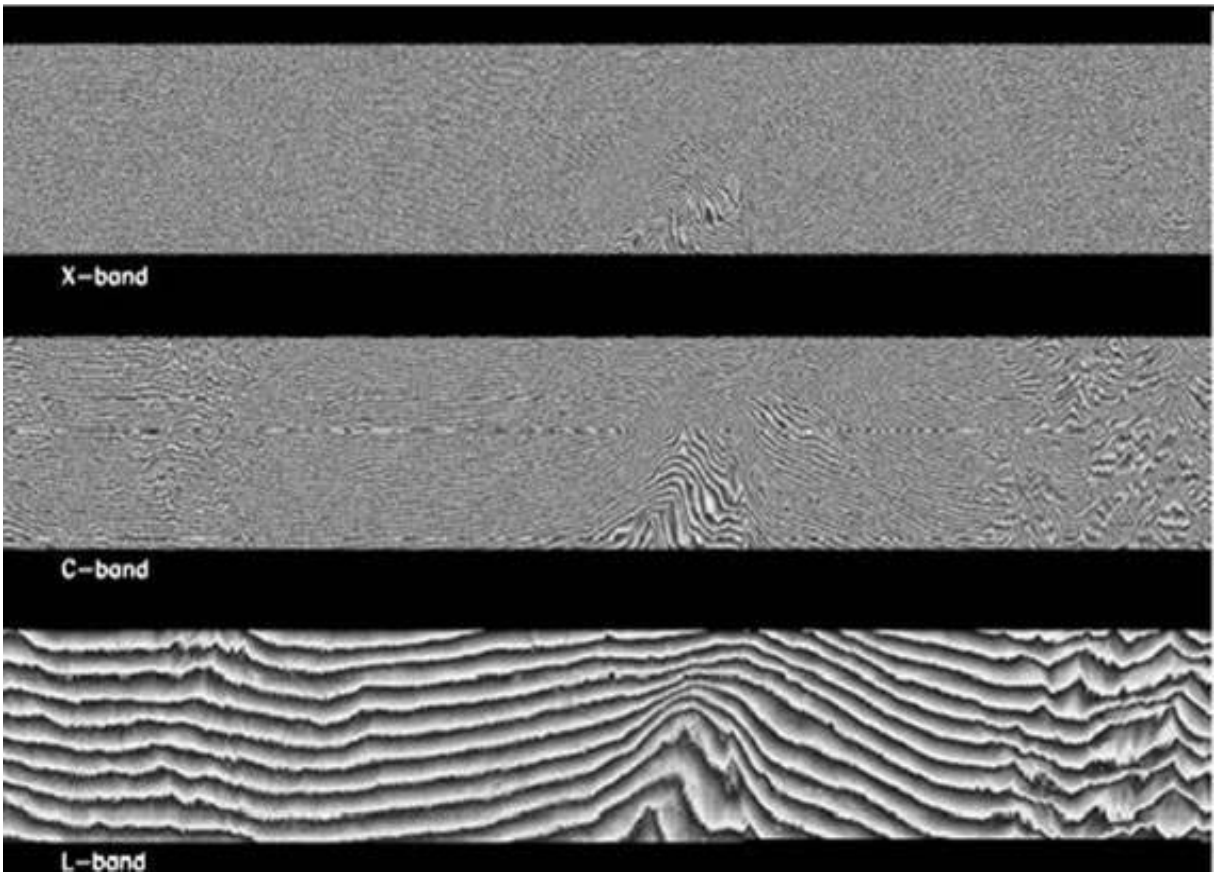

Fig.6 Set of phase fringes without flat earth removal, taken simultaneously in X-, C-, and L-Band with a two pass Interferometry experiment with SIR-C over the Mount Etna Test area. Time difference between the two passes was one day. The Interferogramme after flat earth correction is depicted in Fig 20. (page 21). The area in the left part was relatively flat, the largest slopes of the volcano is nearly in the middle. The image size is 66.8 km in azimuth and 9 km in ground range (16000 radar pulses and 1024 range bins in X-band and 2048 range bins in L- and C-band). More results of the same scene in the Fig. 18 to 24.

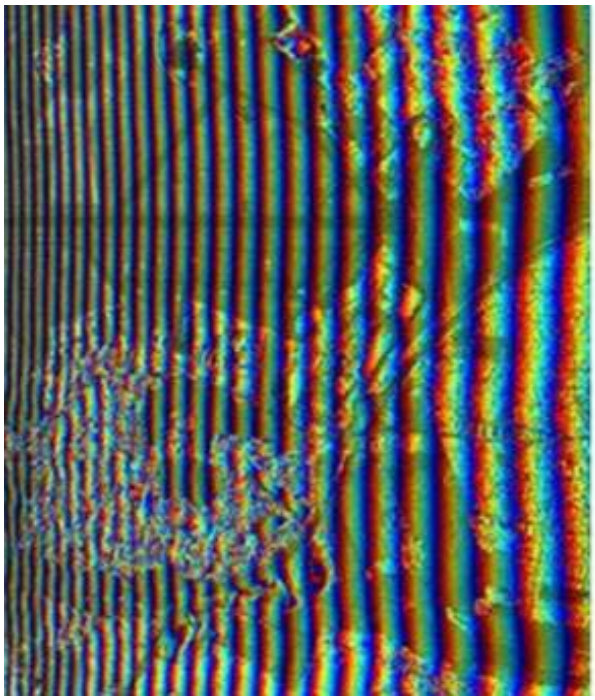

Near Range	Far Range
$\vartheta = 25°$	$\vartheta = 55°$
R = 3530 m	R =5579 m
B = 28.1 m	11,5 m
$2\pi \sim 10{,}3$m Height	$2\pi \sim 49{,}6$m Height
$2\pi \sim 26{,}9$ m Ground Range	$2\pi \sim 105{,}7$ m Ground Range

Fig.7 Example of an airborne Interferogramme, taken with E-SAR in L-band repeat-pass mode in the relatively flat area around Oberpfaffenhofen/Germany. Mainly flat-earth fringes are visible, their frequency changes strongly from near-range to far range.

For the space-borne case with its large altitudes and small incidence angle variations a nearly periodical fringe pattern results with nearly equal fringe width's result. The flat-earth phase is a linear phase ramp. For airborne data the situation is more complicated, the look-angle changes strongly from near-range to far-range, and with it both the observation distance r and the effective base line. Therefore nearly everything gets range-dependent. The flat-earth phase is not a linear phase ramp anymore, it has a curved shape. The height resolution changes with the incidence angle also.

2.3 The Spectral Approach to Interferometry

The relation between the phase of SAR Interferograms and ground elevation is explained as usual by means of geometrical approaches based on the assumption that the RF bandwidth is so small to be negligible. Thus, the system is considered monochromatic. However, if an extended system bandwidth **W** is introduced, a relative shift of the ground wave number spectra dependent on the baseline and the local slope is recognized. Important consequences are revealed from this result. [Gatelli et al. 1994]

1) It can be shown that as the baseline increases and in the absence of volumetric effects the spatial resolution of the Interferogramme is reduced only since the "geometrical de-correlation" can be removed [Prati C., Rocca F., 1993]. Therefore, techniques for improving the Interferogramme quality (i.e., yielding a higher SNR) can be found (with a considerable benefit for phase unwrapping). Moreover, this effect could be completely avoided by means of tunable systems.
2) Rules for the design of pre-summing filters for quick-look interferometric processing can be derived.
3) Repeated satellite surveys can be combined in order to improve the slant range image resolution because the spectra of different signals correspond to different bands of the ground reflectivity's spectrum. The relation between the frequency f and the ground range wave number k_y is given by:

$$k_y = \frac{4\pi}{\lambda} sin(\vartheta - \alpha) = \frac{4\pi f}{c} sin(\vartheta - \alpha) \tag{28}$$

In (28), for simplicity, a constant uniform slope α of the terrain is considered. For the variation of k_y generated by a slight change of the looking-angle $\Delta\vartheta$ follows:

$$\Delta k_y = \frac{4\pi f \Delta\vartheta}{c} cos(\vartheta - \alpha) \tag{29}$$

Thus, in general, a looking-angle difference $\Delta\vartheta$ generates a shift and a stretch of the imaged terrain spectra. However, if the relative system bandwidth is small, the frequency f in the second term of (28) can be substituted with the central frequency f_0.

$$\Delta k_y = \frac{4\pi f_0 \Delta\vartheta}{c} cos(\vartheta - \alpha) \tag{30}$$

From the fact that the radar is not monochromatic, it has a bandwidth W centered around the central frequency f_0 , results that by changing the looking angle of the SAR survey, a different band of the ground reflectivity spectrum shows up.

In order to compare the shift of the ground reflectivity spectrum to the SAR bandwidth W, the ground wave number shift of (30) is expressed as an equivalent frequency shift Δf. The following expression of Δf for an angular separation $\Delta\vartheta$ can be obtained by differentiating (28) directly and taking into account the relations for the small incidence angle changes resulting from Fig. 3:

$$\Delta f = -\frac{f_0 \Delta\vartheta}{tan(\vartheta - \alpha)} = -\frac{cB_{eff}}{R\lambda\, tan(\vartheta - \alpha)} \tag{31}$$

Note: (31) does not state that by changing the looking angle of the SAR survey the radar bandwidth is shifted by Δf, it just says that by changing the SAR looking angle, the backscattered signal contains different spectral components of the ground reflectivity spectrum. The signals received by two SAR's separated by an angle $\Delta\vartheta$ have the same spectral components of the first signal whilst in the second signal the whole spectrum is shifted only by Δf.

A similar result can be demonstrated for the bistatic SAR case where a stereo pair is acquired simultaneously by two sensors: the first is equipped with a transmitter and a receiver, whereas the second is equipped with a receiver only. It can be shown that the spectral shift induced by a baseline B_{eff} is half that obtained in the monostatic case:

$$\Delta f = -\frac{cB_{eff}}{2R\lambda \tan(\vartheta - \alpha)} \tag{32}$$

In the mono static case the two SAR spectra become totally disjoint as the frequency shift Δf equals the system bandwidth W. The critical baseline can be computed as:

$$B_{effcrit} = \left| \frac{WR\lambda \tan(\vartheta - a)}{c} \right| \tag{33}$$

By using the geometric range resolution δ_{rge} instead of the Bandwidth W results from the well known interconnection between range resolution and bandwidth:

$$B_{effcrit} = \left| \frac{R\lambda \tan(\vartheta - a)}{2\delta_{rge}} \right| \tag{34}$$

The Tables 1 to 3 summarize the results obtained in this Chapter, Table 4 is an example for real results.

Tab. 1 Basic Interferometry Formulas

Ground Range:	$y = R \sin\vartheta$ (6)
Local Terrain Height:	$z = H - \frac{r^2 - B^2}{2B\sin(\vartheta - \xi) - 2r} \cos\vartheta$ (7)
Critical Baseline	$B_{effcrit} = \left\| \frac{WR\lambda \tan(\vartheta - \alpha)}{c} \right\| = \left\| \frac{R\lambda \tan(\vartheta - \alpha)}{2\delta_{rge}} \right\|$ (34)
Surface Change Detection Differential Interferometry	$\Delta z = \frac{\lambda}{4\pi} \Delta\Phi$

Tab. 2 Parameter Examples for Interferometry with a space-borne SAR from ERS/ASAR Type

Input parameters	**Value**
• velocity: v	7.464 km/s
• range delay (mid swath): T_0	5.779 ms
• slant range (mid swath): R_0	866.656 km
• incidence angle (mid swath): ϑ	23°
• altitude: H	794 km
• wavelength: λ	0.0566 m
• baseline tilt angle: ξ	0°
• baseline length: B	200 m
• surface slope: r_x	r_y
• phase error: $\Delta\Phi$	5°
• baseline length error: ΔB	0.001 m
• baseline tilt angle error: $\Delta\xi$	1°
• slant range error: ΔR	3 m
• height error: ΔH	1 m

Tab. 3 Resulting Errors for absolute Height Estimation

Error Type	Formula	Errors
Phase	$\Delta z_{\Phi} = \frac{\lambda R \sin\vartheta}{4\pi B \cos(\vartheta-\xi)} \Delta\Phi = \frac{\lambda R_g}{4\pi B_{eff}} \Delta\Phi$	$\Delta\Phi$=5° ➔ Δz_{Φ} 0,723m
Baseline Length	$\Delta z_B = -R \tan(\vartheta - \xi) \sin\vartheta \frac{\Delta B}{B}$	ΔB = 0,001 m ➔,Δz_B = 0,719 m
Baseline Tilt Angle	$\Delta z_{\xi} = -R_0 \sin\vartheta \Delta\xi$	$\Delta\xi$ = 1° ➔ Δz_{ξ} =5910,20 m
Range Delay	$\Delta z_R = -\cos\vartheta \Delta R$	ΔR = 3 m ➔ ΔT = 0,2 µsec ➔ Δz_R = -2,762 m
Altitude	$\Delta z_H = \Delta H$	ΔH = 1 m ➔ Δz_H = 1m

Tab. 4 Digital Elevation Model errors caused by instrument inaccuracies of SRTM/X-SAR. Goal was a relative height accuracy (90 %) < 6 m absolute height accuracy (90 %) < 16 m [Keydel et al 2000]

DEM Error Examples for SRTM (Middle of Swath)				
	Relative (30 seconds)		Absolute (11-days)	
Error Type	Inaccuracy	DEM-Error	Inaccuracy	DEM-Error
Baseline Tilt Angle	2 arcsec	3,0 m	9 arcsec	13,4 m
Baseline Length	1,3 mm	0,8 m	4,0 mm	2,6 m
Instrument Phase	4,0deg	4,2 m	4,0 deg	4,2 m
Total (RSS)	5.5 m		14.4 m	

Conclusions

Absolute height measurement with interferometric SAR requires an extremely stable system performance. Especially the orbit has to be known very precise due to its great impact on the baseline length, the tilt angle accuracy and the altitude accuracy. An instrument phase error of 5° leads to an error in the height estimation of about 1.5 m in the mid swath and, therefore, seems to be acceptable.

3. Coherence and Correlation in SAR Interferometry

For SAR Interferometry the coherence between two signals to be compared defined in the Introduction Lecture is a fundamental parameter. The Coherence is a measure for the quality of Interferogrammes. Equation (4) will be used to produce the complex SAR-Interferogramme replacing the Fields E_1 and E_2 by the complex Images I_1 and I_2 gained in each of the two Interferometry channels. This Interferogramme is defined as the product of the complex SAR values of the second image with the complex conjugate of the reference image. Principally, the Interferogramme is the complex Coherence Image C_{image}:

$$C_{image} = \frac{\left\langle (I_1(t) I_2^*(t)) \right\rangle}{\sqrt{\left\langle I_1(t) I_1^*(t) \right\rangle \left\langle I_2(t) I_2^*(t) \right\rangle}} \tag{28}$$

The corresponding amplitudes have to be averaged and the corresponding phases have to be differenced at each point in the image. The resultant phase of the Interferogramme, which is directly related to the topography, is measured modulo 2π only. To calculate the elevation of each point it is, therefore, necessary to add the correct integer number of phase cycles to each phase measurement. The method of solving this ambiguity is called phase unwrapping.

On that basis applications of interferometry can be split into two categories, based on whether the main parameter of interest in the complex interferograme is the phase (4) or the magnitude (5) of the complex coherence, Fig 8.

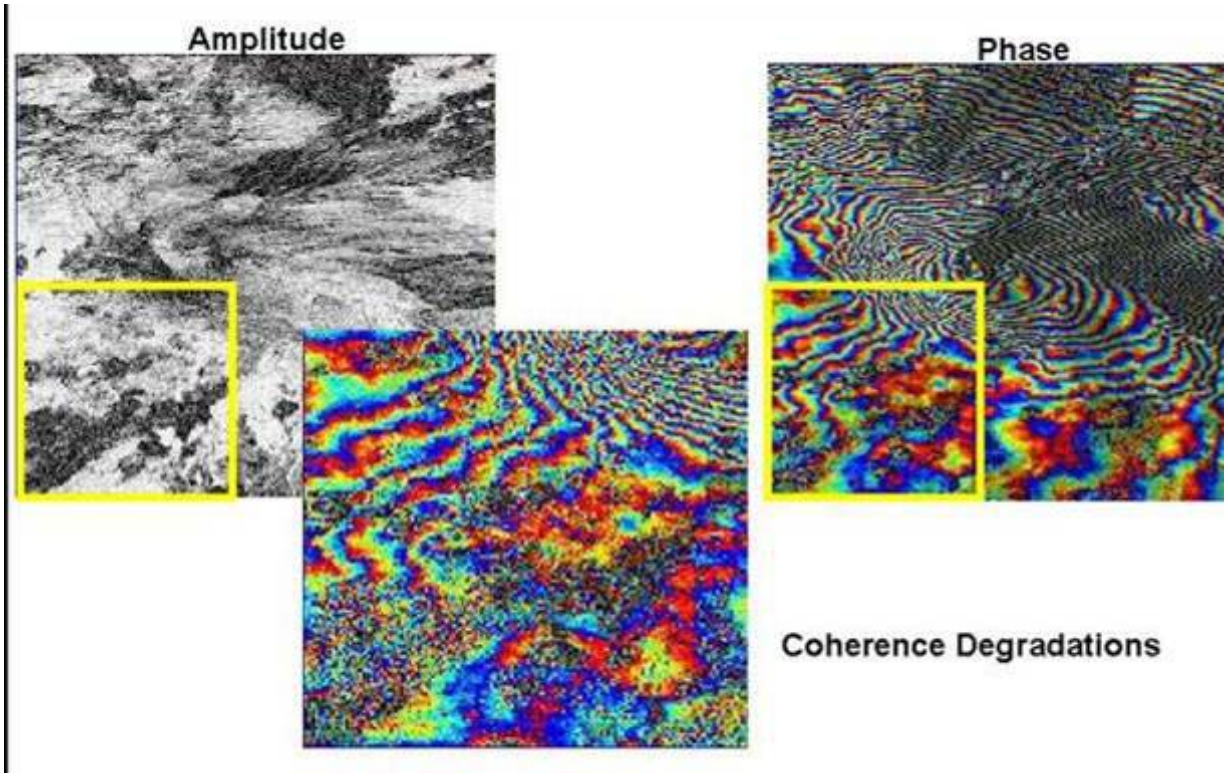

Fig.8 SIRC result, L-Band. Example for fringe degradation due to coherence loss caused by temporal decorrelation in the Mount Etna area which is covered by vegetation in the yellow Square.

The phase information can be used for Digital Elevation Model (DEM) production, provided the scene is relatively stable. For repeat-pass Interferometry, the phase may also be used for studying small coherent motions of the target between the imaging times, a motion in which most of the scatterers move simultaneously. This finds applications in geological studies of land motion (e.g. associated with seismic activity or land slip), and in glaciology. The accuracy of the measurements of height and motion are in part determined by the noise of the phase measurements. This phase noise is usually characterized by the magnitude of the coherence of the Interferogramme, often simply referred to as the coherence.

Important information can be extracted from images using the coherence. This is true for land use classification, where the information obtained is complementary to the intensity of the SAR images, and may give, for example, better discrimination between clear cuts and forest areas than intensity measurements. Another use of coherence in this respect is the monitoring of changes to land surfaces (e.g. harvesting of agricultural crops). Fig 9 shows an example for Land classification obtained with coherence evaluation of a multi frequency X-SAR/SIRC result; the respective phase image of that very scene without flat earth removal is depicted in Fig.6 (page 8).

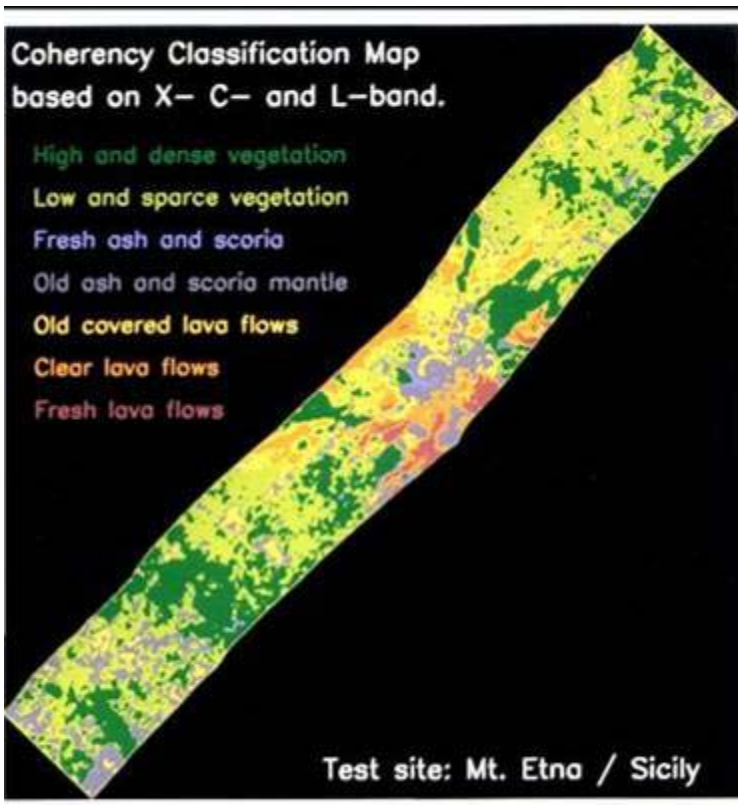

Fig. 9 SIR-C Classification result of the Mount Etna test area obtained with coherence comparisons in L-, C-, and X-Band

There are a number of causes for de-correlation in Interferometry, and it is possible to write the coherence as a product of factors which give some physical insight into the origin of the de-correlation:

$$\gamma = \gamma_{instrument}\ \gamma_{processor}\gamma_{baseline}\gamma_{azimuth}\gamma_{noise}\ \gamma_{temporal}\ \gamma_{spatial}$$

The first three terms are totally independent of the target being imaged, the fourth and fifth are related to both the system and the target, and the final term is totally dependent on the target properties as will be explained.

$\gamma_{instrument}$ refers to both Radar and Platform

$\gamma_{processor}$ refers to effects produced during the processing of the SAR images to form the Interferogramme and includes, for example, miss-registration of the images when aligning them before forming the Interferogramme and overlap of the range and azimuth spectra. The latter means the two surveys must image the scene under the same squint angle, they have to have the same Doppler Centroid. The to days processing routines are estimated to register the two images to within one hundredth of a pixel in both range and azimuth, leading to a negligible loss of coherence.

$\gamma_{azimuth}$ is a factor introduced to account for differences in the Doppler Centroid frequencies between the two images. For repeat-pass Interferometry exemplary with the ERS-1 or RadarSAT-1 satellites this effect is negligible as the high stability means that the Doppler centroids typically vary by only about 0.02 of the sampling frequency.

γ_{noise} represents the effect of noise in the system is well known and can be expressed as

$$\gamma_{noise} = \frac{CNR}{CNR+1} = \frac{1}{1+CNR}$$

where CNR denotes the clutter-to-noise ratio. This is important for regions of weak backscattering.

$\gamma_{temporal}$ refers to the de-correlation in single pass Interferometry which depends simply on the factors discussed above. In the case of repeat pass Interferometry, where the time interval between images may be days

or longer, there is also a contribution to the de-correlation due to the possibility of changes in the scatterers themselves and due to the changes of weather conditions in the propagation path. An agricultural field for example de-correlates steadily with the evolution of the crop. The correlation is completely destroyed once the field is ploughed. Forests de-correlate even more rapidly etc. On the other hand many manmade and natural objects prove to stay coherent over years and decades which enables the techniques of Permanent Scattering Interferometry considered in Chap.7

$\gamma_{baseline}$ refers to the baseline of the two passes which has to be smaller than the critical effective baseline

$\gamma_{spatial} = \gamma_{range}\,\gamma_{volume}$ refers to the de-correlation caused by different acquisition look angles

γ_{range} refers to the de-correlation due to different projections of the bandwidth onto ground

γ_{volume} refers to the de-correlation related to the height distribution of the scatterers

In Fig. 8 the influence of coherence degradations on the Interferogramme is depicted. It is impossible to apply the definition of coherence directly to the SAR images, due to the fact that it involves ensemble averaging. In practice an assumption is made in which a spatial average is taken to be a reasonable approximation of an ensemble average. This requires that phase variations between the pixels being averaged have been corrected for topographic variations. The averaging process introduces a bias into the coherence measurements, the level of which is determined by the number of independent samples used.

However, the coherence of a pair of interferometric images gives one indication of the quality of the obtained Interferogramme [Monti 97]. Also the coherence matrix is a basic starting point for some unwrapping algorithms. If real time is desired, or an increment in the speed of all the chain from raw data to the digital elevation model (DEM) is needed, the time reduction in computing the coherence should be undertaken.

The usual coherence estimator needs to calculate the local frequency of the interferometric fringes very accurately and therefore this algorithm becomes very time consuming. The coherence between two complex SAR images I_1 and I_2 is given by (28). Assuming stationary regions and ergodicity (i.e. all scatterers within the estimation area are independent with identical statistical properties), the coherence can be calculated with high accuracy as:

$$\gamma_{est} = \frac{\left| \sum_{n=0}^{N} \sum_{m=0}^{M} I_{1(n,m)} I_{2(n,m)} e^{-j\Phi(n,m)} \right|}{\sqrt{\sum_{n=0}^{N} \sum_{m=0}^{M} \left| I_1(n,m) \right|^2 \sum_{n=0}^{N} \sum_{m=0}^{M} \left| I_2(n,m) \right|^2}} \tag{29}$$

γ_{est} is called coherence estimator. N and M give the size of the estimation window in range and azimuth. The factor The inclusion of a factor of $e^{-j\Phi(n,m)}$ is due to the difference between the two SAR images, which differ by the deterministic phase, that should be estimated and corrected.

4. Generation of Interferometric Products

4.1 Interferometric Product Generation Principle

The input data used for SAR Interferometry are the complex SAR image pairs and the respective navigation data. The procedure used for the generation of the interferometric products is depicted in Fig.10 and can be summarized as follows:

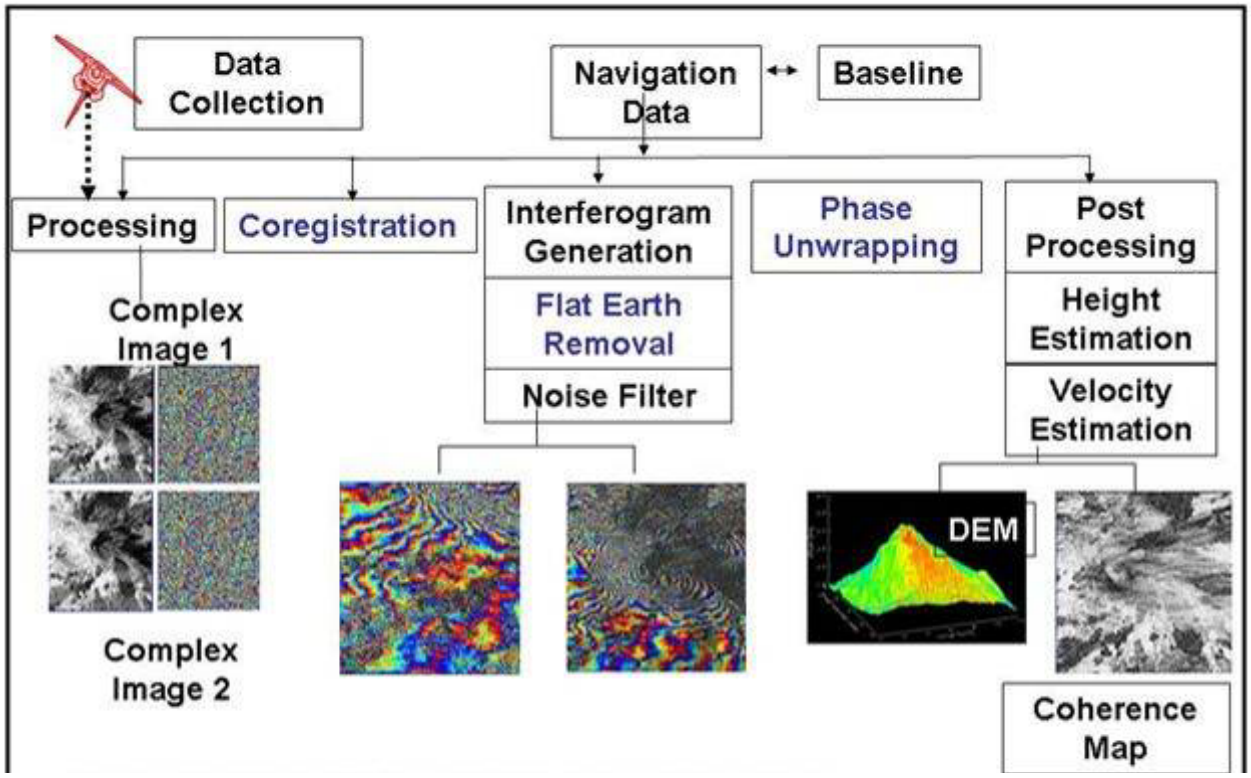

Fig. 10 Principal procedure used for the generation of interferometric products, exemplary DEM's and coherence maps.

1. Processing including range and azimuth filtering of the complex images. Before the Interferogramme is formed, the complex image pair has to be filtered separately in both range and azimuth directions to optimize the coherence and the interferometric phase purity. The so-called spectral shift range filtering will be applied in order to minimize baseline-induced de-correlation. Filtering to a common Doppler band in the azimuth direction will be applied to eliminate the de-correlation effect induced by the Doppler Centroid difference between the two images [J. Moreira, M. Schwäbisch,et.al 1995].
2. Coregistration. In order to obtain the interferometric phase, the image pair has to be co-registered. This has to be carried out with a high degree of accuracy; state of the art is the order of one hundredth's of a pixel.
3a. Interferogramme generation. The Interferogramme is generated by multiplying the first image, L , with the complex conjugate of the second image, referred to as I_2
3b. Flat-earth phase removal. To perform the Interferogramme noise filtering and simplify the phase unwrapping procedure, a first-order, flat-earth phase removal is carried out. The flat-earth phase is computed by measuring the dominant fringe frequency in the azimuth and range directions of the Interferogramme. It thus consists of two different linear phases in the range and azimuth directions..
3c. Phase noise reduction. In order to reduce the phase noise and to facilitate the phase unwrapping, the Interferogramme has to be filtered using an averaging window with a size of several resolution elements in both range and azimuth. Respective pixel spacings and resolutions used for X-SAR processing are shown in Table 1 exemplary. After the filtering, the interferometric phase is determined by calculating the arctangent of the Interferogramme. The terminology and respective procedures are given in the next sections.
4. Phase Unwrapping, the most important procedure will be deeper described in subchapter 4.2
5. Post Processing with height and velocity estimation ending up with the desired DEM and a coherency map of the scene.

4.2 Phase Unwrapping

Phase Unwrapping is the key procedure for SAR Interferometry data evaluation with respect to establishing DEM's. Meanwhile, there are many methods for the two dimensional Phase unwrapping. The very basic principle is depicted in Fig.11 for a simple one dimensional case which is self explaining.

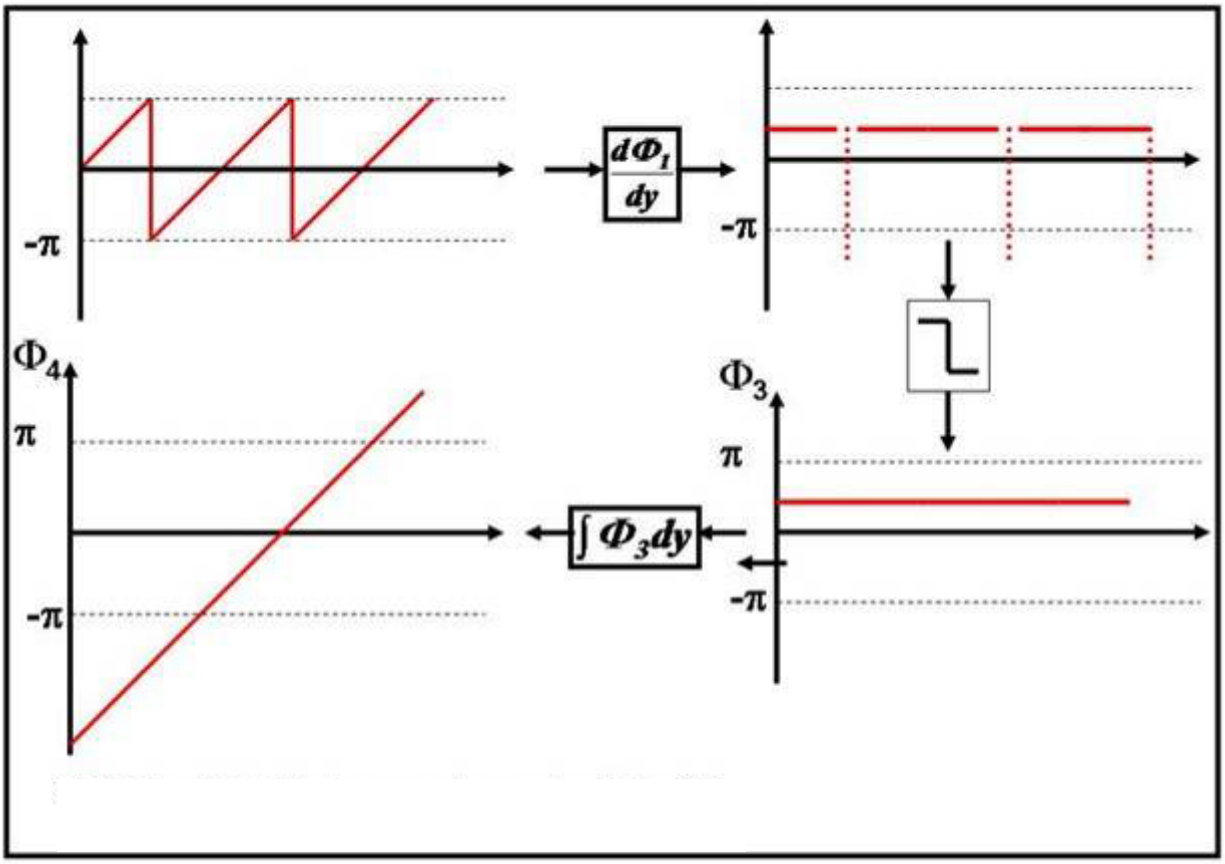

Fig 11 Basic principle of the phase unwrapping procedure, Reigber 2001

A more sophisticated principle is the least square-Method which minimizes the differences between the derivatives of the wrapped and unwrapped phase functions using the fact that the minimum of the first derivative is determined by the null of the second derivative. In the two dimensional case the partial differential quotients have to be used. This method seems to be very simple and fast. However, the errors are propagating very strongly down to the entire sequence and therefore, this method is not very practicable for large area processing.

As further examples branch cutting, fringe detection, and knowledge injection should be mentioned in a bit more detail despite of the fact that they don't represent the most modern state of the art. However, they seem to be important to gain insight into the whole complex. [Gens R., 1996]

Branch cutting

The first method, which is based on creating so called *branch cuts* was developed in 1988 already by Goldstein *el al.* They pointed out that there are two possible types of errors in the unwrapped sequence. The first are local errors in which only a few points are corrupted by noise; the second are global errors in which the local error may be propagated down the entire sequence. The global errors arise from the residues. Residues are local errors in the measured phase caused by the noise in the signals or by actual discontinuities, i.e., layovers, in the data. There are three major sources of noise. The first is thermal noise, the second is the speckle, which is a random variable, and the third one is caused by an antenna effect depending on the antenna separation, the bandwidth of the radar, and the geometry of the image formation. Assuming that the original scene is sampled often enough so that the true phase will not change by as much as one-half cycle per sample point the phases can be unwrapped in a consistent manner. This can be done if the residues are identified and suitable branch cuts are made between the residues to prevent any integration path from crossing these cuts. Filtering the signal will reduce the residues in the image but it also reduces the spatial resolution in the final topographic map. Before integrating the phase differences all residues which were previously low-pass filtered are to connect with branch cuts. The phase differences are then integrated without crossing any of the cuts.

Fringe detection

Another method for the two-dimensional phase unwrapping is the fringe detection method of Lin *et al.* (1992). The first step in this method is to find the location of the fringe lines in the phase difference image by using edge detection techniques which mostly include the two steps of enhancement by filtering and then applying a threshold to the image. The phase difference image is median filtered with a window size which depends on the density of the fringes. For the detection of the fringe lines, five edge masks with different orientations are applied. The phase is then unwrapped by adding a multiple of 2π each time the integration path crosses a fringe line. The multiple depends on how many fringe lines lie between the pixel and a reference pixel. The solution is considered good when the fringes are greatly separated and the signal-to-noise ratio (SNR) is high in the entire wrapped phase image [Hartl et al.1993].

Knowledge injection

This method is used for reducing the density of fringes by incorporating the use of a rough DEM. [Adragna 1995]. The same technique is also used for flat Earth removal, and for differential Interferometry (Chap..5.), in which knowledge of the topography is injected to isolate the terrain movement. It should be noted that all the methods of phase unwrapping described above are generally performed after flat earth removal.

4.3 Co-Registration

The co-registration is a very important processing step in Interferometry also. For distributed scatterers, a co-registration inaccuracy introduces substantial noise into the interferometric phase (Bamler et al., 1993), and point scatterers have to deal with a systematic phase error (Holzner et al.,2001). (Compare the PSI considerations in Chap.7 also). Bamler (2000) showed that the error of the co-registration parameter estimation for distributed scatterers depends on the number of correlation points n and the coherence γ:

$$\sigma_{corr} = \sqrt{\frac{3}{2n}} \frac{\sqrt{1-\gamma^2}}{\pi\gamma}$$

The dimension here is the unit of the resolution cell. Accordingly, in order to guarantee appropriate co-registration accuracy in low coherence scenes the correlation window size needs to be increased. However, the co-registration still strongly depends on the temporal coherence and the co-registration limit is often insufficient.

5. Along-Track Interferometry for Velocity Determination

The arrangement of the two antennas in cross velocity direction is essential for topographic mapping because that arrangement only leads to phase differences between the two SAR images. An along track arrangement as depicted in Fig.2 (page 3) would produce two identical images with no phase differences at all due to the same processing procedure. Each object had both the same distance and the same Doppler Frequency with respect to the two receiver ore antennas respectively. However, there is a time shift T between the two images due to the fact that both antennas pass the point of nearest approach to each pixel - which is the locus of Doppler Frequency 0 - in a sequence which is dependent on Baseline length and platform velocity v_{plat}.

$$T=B/v_{plat}$$

A target changing its position during that time with the velocity v_{targ} will change its position in the second image in accordance with its own velocity producing a phase difference Φ. The Phase difference between corresponding pixels is a measure for the velocity of the object in the scene. This procedure is called Along Track Interferometry.

$$\Phi = m \frac{2\pi}{\lambda} v_{targ} T = m \frac{2\pi}{\lambda} \frac{v_{targ}}{v_{plat}} B \tag{30}$$

In order to determine the ground range velocity V_{targy} of a target ore a pixel respectively which is moving on ground neglecting the vertical velocity component $v_{targ\,z}$ for simplicity reasons results:

$$V_{targ\,y} = \frac{V_{targ}}{\sin \vartheta} \tag{31}$$

The measurement of the velocities of different resolution cells of water surfaces for instance allows the estimation of water currents with respect to both current velocity and the respective direction. However, the along-track technique will not be suitable for the measurement of along track velocity components. But with two separate measurements in cross directions a two dimensional current map can be established. Fig. 12 shows an example. In Fig. 13 results of moving target detection and measurement results are depicted. Here, additional a priori map information with respect to position and direction of the respective roads within the scene has been used assuming that the identified vehicles were driving on roads only.

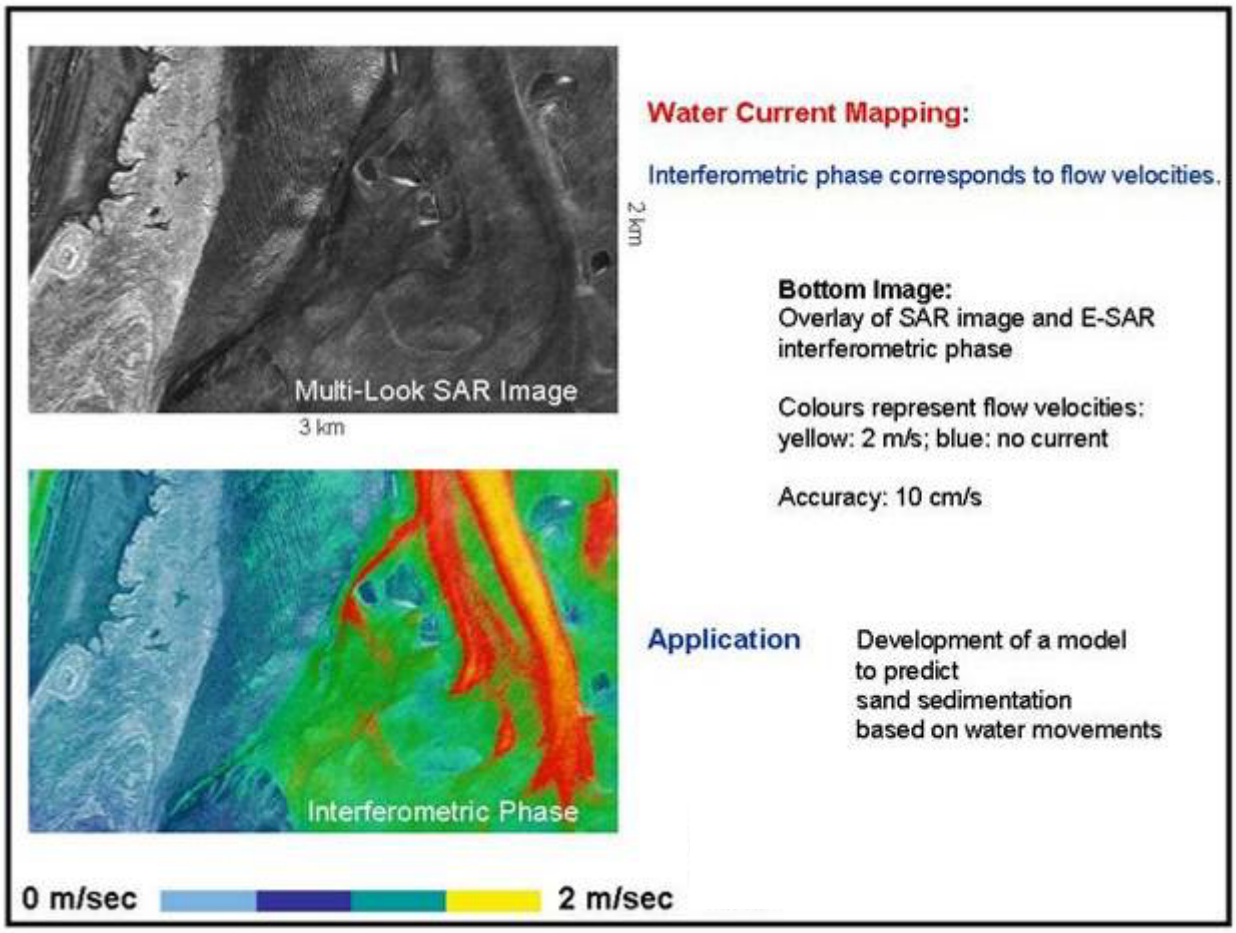

Fig. 12 Example for current velocity measurements with along track interferometry. The colours represent flow velocities, :yellow: 2 m/s; blue: no current

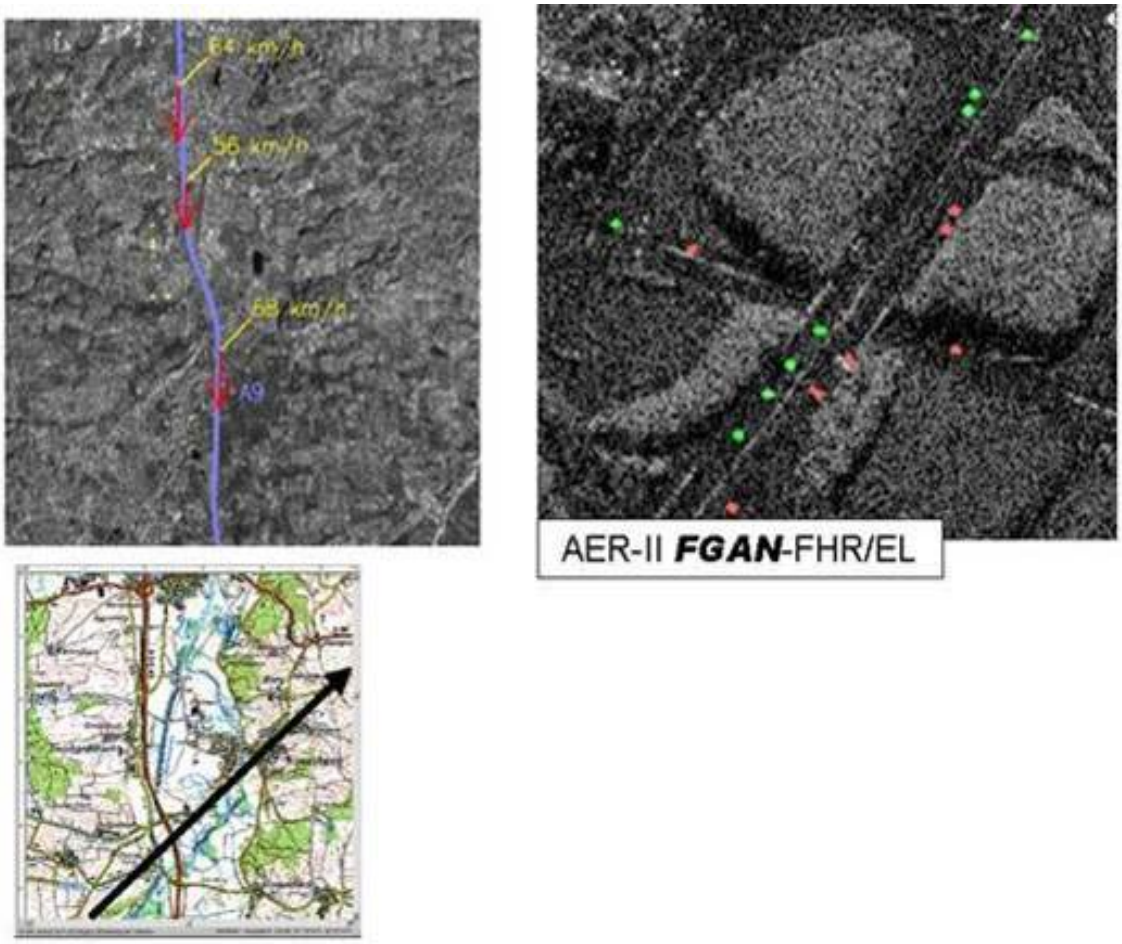

Fig. 13 Examples for MTI with space borne (left) and airborne (right) along track Iinterferometry.
Left: X-SAR/SRTM one pass Interferometry image, baseline 7m. Motorway A9, Munich – Nuremberg, Germany, motorway blue, red arrows vehicles with their velocities (yellow) , black arrow: SRTM track [Breit et.al.2003]. Right: airborne one pass Interferometry image with vehicles in two directions on the highway [Ender 1996]

6. Differential SAR Interferometry

Many operational monitoring tasks require the detection of changes during a certain time period. This can be performed with Differential SAR Interferometry which registers the respective topographic changes of a DEM which happened during the time period since the DEM has been established. There are principally two techniques depending on the availability of pre-existing digital topographic maps.

If such a DEM with acceptable accuracy is available then it has to be subtracted from the DEM which results from the interferometric phase field measurements. The difference between the two DEM's represents the changes to be determined.

If no digital topographic maps are available then two Interferogrammes of the same area have to be taken over the desired time period. The first one is used to generate a reference Interferogramme and the second one to generate a Interferogramme which contents both the reference DEM together wit the changes to be monitored. This leads to a double-difference interferogram, which can be derived from the two corresponding Interferogrammes by subtraction of both Interferogrammes.The phase discontinuities in the two Interferogrammes will not occur in the same places. Therefore, each Interferogramme must be unwrapped.

The sensitivity of SAR Interferometry depends on the geometry of the observation and can be increased at the expense of spatial resolution by averaging over more pixels. The length of the baseline in relation to the wavelength used has an influence on the amount of noise which is introduced. A decreasing baseline ore an increasing wavelength leads, therefore, to a higher accuracy of the detected height differences.

The principal geometry for the space borne two pass mode is depicted in Fig 14. For simplicity reasons in describing the principles it is assumed that both Interferogrammes use the same primary flight path, however they can have different baselines. The following Interferogrammes will be obtained:

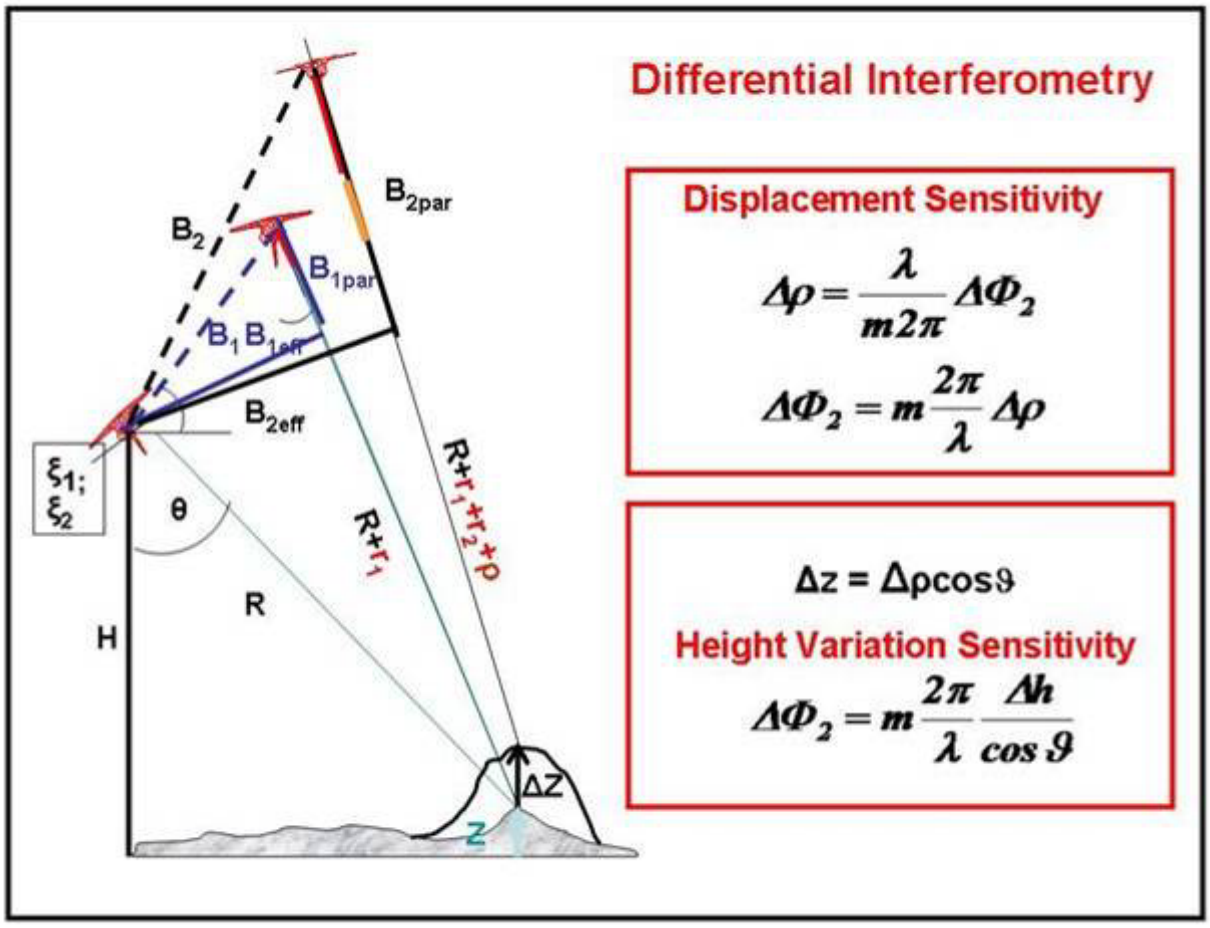

Fig.14 Differential Interferometry Principle

Interferogram 1:

$$\Phi_1 = m\frac{2\pi}{\lambda}r_1 = \Phi_{topography} = m\frac{2\pi}{\lambda}B_{1\,par} \tag{32}$$

Interferogram 2:

$$\Phi_2 = m\frac{2\pi}{\lambda}r_2 + m\frac{2\pi}{\lambda}\rho = \Phi_{topography} + \Phi_{displacement} \tag{33}$$

The subtraction of (32) from (33) leads to the displacement in line of sight direction

$$\Phi_2 - \Phi_1 = \Phi_{displacement} = m\frac{2\pi}{\lambda}\rho \tag{34}$$

This expression is not dependent on the topography anymore. As explained in Cap. 2.2 the sensitivity results from differentiation which leads to

$$\Delta(\Phi_2 - \Phi_1) = \frac{2\pi}{\lambda}\frac{\Delta z}{\cos\vartheta} + \frac{\Delta y}{\sin\vartheta} \tag{35}$$

Fig 15 shows exemplary the displacements caused by an earthquake in Japan.

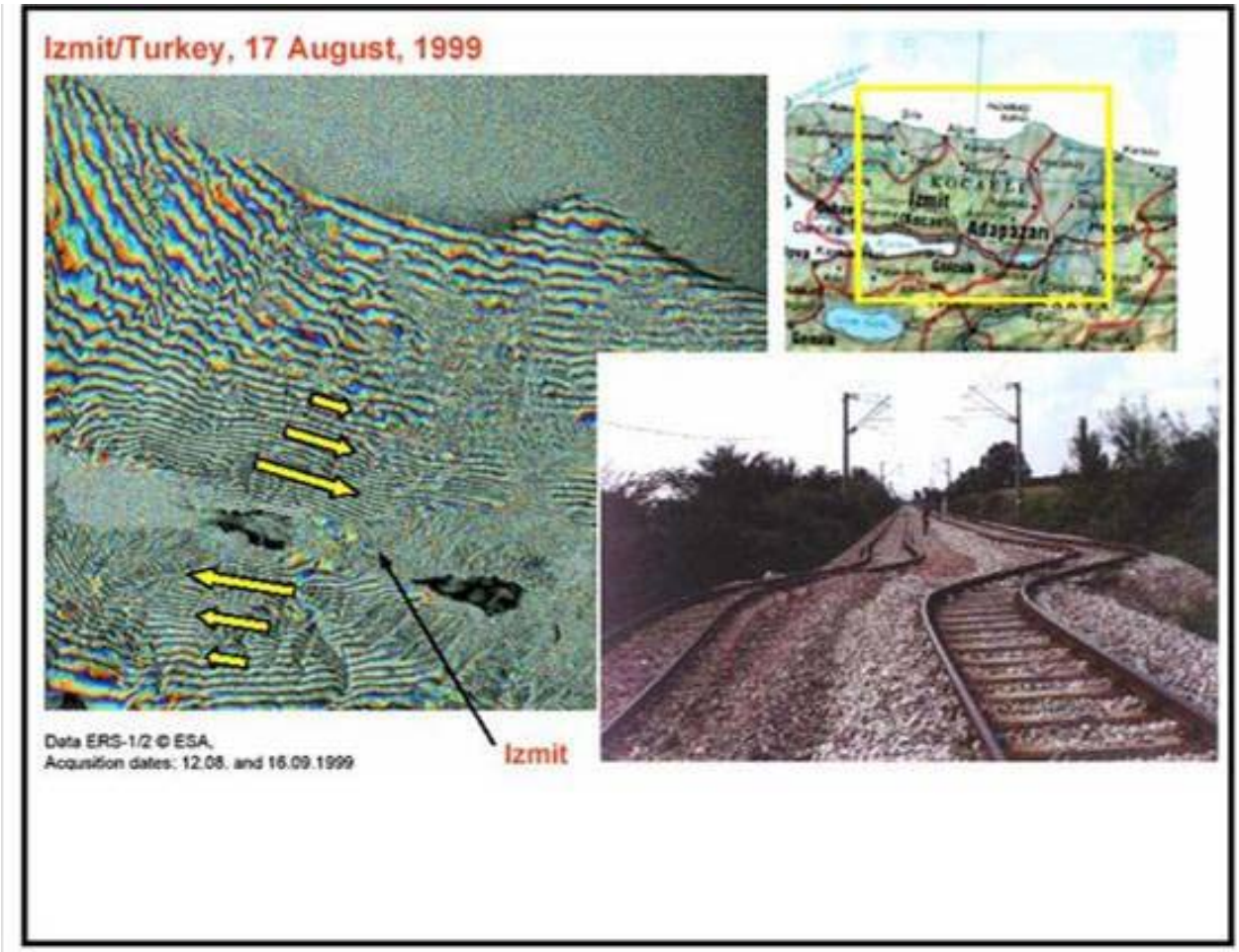

Fig.15 Differential Interferometry result., displacement pattern caused by an earthquake [http://comet.nerc.ac.uk/schools_eq_izmit.html and Bamler, 2000]

7. Permanent Scatterer Interferometry (PSI)

Differential Interferometric SAR over longer time periods is often limited by temporal de-correlation. As mentioned already many manmade and natural objects prove to stay coherent over years and decades. These so-called Permanent Scatterers (PS) can be used for the ultimate sensitivity in motion measurement from space (Ferretti et al., 2000; Ferretti et al., 2001) by using them as points of reference. PS's are usually bright points in the image, with a very high signal-to-noise ratio. However, the phase information itself cannot be used for detection of stable points, since it contains phase uncertainties induced by unknown elevation and deformation but amplitude time series can be well used for this [Ferretti 2001]. The permanent Scatterer technique uses a sequence of many Interferometric SAR products of the same area of interest taken over a long time period establishing in a first step a data base of very many SAR images. From the observed phase time series of the differential Interferogrammes the elevation difference and deformation rate difference over time can be determined.

Presently such databases are available, principally, from the most areas of the globe taken from different operational satellites like ERS-1/2, RadarSAT-1, J-ERS etc. which where in orbit permanently since more than 15 years. (Some of them will be numbered and considered in the Systems chapter of this very lecture Series).

If several SAR images are superposed, even the propagation errors due to tropospheric water vapour can be averaged out. In practice 30 – 100 SAR images of the same areas are used to form an interferometric stack spanning a time period of typically 5 – 12 years. In this co-registered stack, the PS's are identified and their phase history can be tracked and analysed. Several filtering and adjustment steps are required to remove orbit

errors, long-wavelength ionospheric delays and to reduce atmospheric effects and noise. The result is a map of subsidence/inflation rates to an accuracy of less than 1 mm/year.(Bamler, SRTM and beyond)

If, for example, n + 1 ERS SAR images from one certain area are available the data will be first co-registered on a unique master and a first DEM of the area will be established as a reference. Then, n differential Interferogrammes between all SAR images and the master will be computed. After DEM compensation, the residual phase Φ_i of the Interferogramme number i is:

$$\Phi_i = \frac{4\pi}{\lambda} r_i(T_i) + \Phi_i^{atm} + \Phi_i^{noise} + \Phi_i^{topo} + \Phi_i^{displacement} + \Phi_i^{orbit} \qquad i = 1..n \qquad (36)$$

r_i (T_i) represents the momentary target position at the time T_i and herewith, principally, the possible target motion in the line-of-sight direction, Φ_i^{atm} is the atmospheric phase contribution, Φ_i^{decorr} the contribution of the de-correlation noise, Φ_i^{topo} is the topographic phase error etc. All errors are mentioned already in Chap.2.2,

A time series analysis of the first term in equation 1 reflects the target motion: here for simplicity a constant velocity model is supposed. An uniform strain rate hypothesis is often used in geophysical modelling; however, more complex models can be adopted if the linear model is unrealistic. Permanent scatterers are characterized by low phase residues and are determined by

$$\frac{\partial}{\partial T}\left(\frac{4\pi}{\lambda} r_i(T_i)\right) = 0$$

The first term in equation (36) can be written as follows:

$$\frac{4\pi}{\lambda} r_i = \frac{4\pi}{\lambda} V_r T_i = C_{Vi} V_r \qquad i=1\ldots\ldots\ldots n \qquad (37)$$

V_r is the unknown component of the target velocity m in the Line of Sight (LOS) direction and T_i is the temporal baseline between the master acquisition and the generic i-th slave image. Since there are n differential Interferogrammes of the same area with different temporal and geometric baselines, a linear system of n equations and, principally 2 unknowns (the velocity V_r and the DEM-quantities) is established and a joint estimation of both DEM errors and target velocity can be carried out on a pixel-by-pixel basis. In order to reduce the effect of atmospheric patterns and compensate for baseline errors, the low frequency components should be previously removed from Φ_i. The processing is then performed on a pixel-by-pixel basis and the final result is a velocity field of the area of interest together with an improved DEM. In order to compensate for possible baseline errors and/or very low frequency spatial phase distortion due to atmospheric inhomogeneities the linear component of the residual phase values was removed from all the available data.

Fig.16 shows the principal structure of an overall PSI system. (Adam, et. al. 2003).

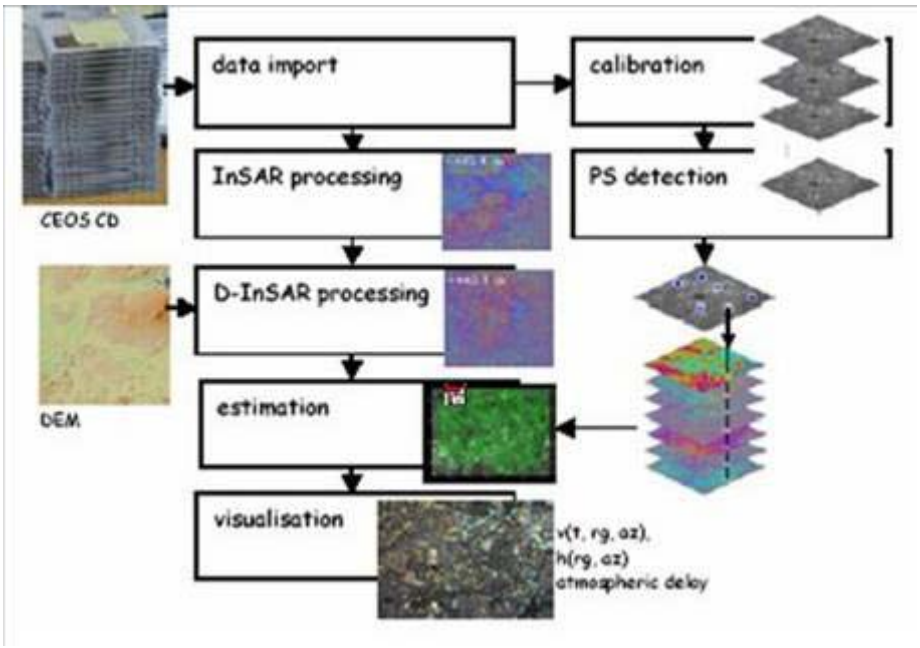

Fig 16. The structure of the overall PS system of DLR.
Each box illustrates a sub-processing system.

The meaning and the tasks of the single Boxes are as follows:

The **Data Import box** starts the initial data setup and selects the area of interest. The **InSAR processing box** represents the normal Interferometry processing procedure. The master scene is selected in order to start the **InSAR Processing**. Parameters as the effective baseline, the acquisition date, the Doppler Centroid frequency and the season of the acquisition form the selection criteria. During the InSAR processing the observation of geometry parameters as the height-to-phase conversion factor, the flat-earth phase, the range distances and the look angle are computed. Furthermore, the scenes are co-registered and re-sampled with respect to the master scene and the Interferogrammes are generated. Because of the utilisation of point scatterers, a spectral shift filtering is not necessary.

In the **Differential Interferometric Processing** module the observation geometry of the radar acquisition is simulated. A DEM and precise orbits are used as input in order to correct for the Interferogrammes. Any available DEM can be used to reduce the topographic signal. Exemplary the DEM's generated from the X-SAR shuttle mission can be used ore a DEM derived from the ERS tandem mission. This module also determines the co-registration and, therefore, it can be used for that processing step also. With the PS Interferometry, the co-registration becomes more difficult than in normal Interferometry considered in Chap.4. The reason is the long time separation (up to ten years) between the acquisitions and the immense temporal de-correlation in non-urban areas.

The σ_0 **calibration** of the scenes has to be introduced for the PS detection. To analyse the temporal back-scattering behaviour of the point scatterers it is necessary to compare their intensity by the calculation of the radar cross section. This module corrects for the processor gain constant, the antenna pattern and the range spreading loss. The **Permanent Scatterer Detection** and identification is performed in the co-registered calibrated scenes by a homogeneity test (Ferretti et al., 2001). Aim is to find as many scatterers as possible because a subsidence pattern and the atmosphere have to be sampled spatially as dense as possible. However, unreliable points causing incorrect estimation have to be avoided. Therefore, the temporal analysis of the differential phases is restricted to point scatterers with a high SNR and a long-time stable backscattering behaviour. These are usually man-made features (Usai et al., 1999) and have to be detected in the scene. The extraction of the PS information reduces the amount of data from more than 100 GB to less than 300 MB. Range and azimuth position of the scatterers in the scene, the calibrated intensity , the look angle, the Doppler Centroid frequency, the height-to-phase conversion factor, the temporal baseline, the scatterer sub pixel position and the differential phase in a compact form are the result from this processing step which can be considered as a raster to vector converter.

Both modules Estimation and Visualisation: The measured differential phase is composed of contributions from the uncompensated topography Because the phase is measured modulo 2π a non-linear inversion problem is given. It is solved by utilising the different behaviour of the contributions regarding the acquisition parameters effective baseline, temporal baseline, range and azimuth location of the scatterers. The **visualisation box** visualises the different spatial properties for a subsidence, for an orbit error, for the atmosphere and for noise. A relative estimation between point scatterers located closely to each other reduces the influence of the atmosphere and of orbit errors. Utilising a periodogram a constant relative subsidence rate can be estimated. These relative estimates are transformed into a global subsidence map by a 2-D integration procedure based on a LS-adjustment.

Fig.17 shows a section of a radar image of Berlin. The PS's are marked by coloured dots, the colours represent the subsidence rate. A second example is shown in Fig.18. The area around the Olympic stadium in Berlin is subject to ground water regulation activities. This area shows up as red PS's, i.e., the ground level is lifting by about 3 mm/year. During the lecture on applications additional examples will be discussed.

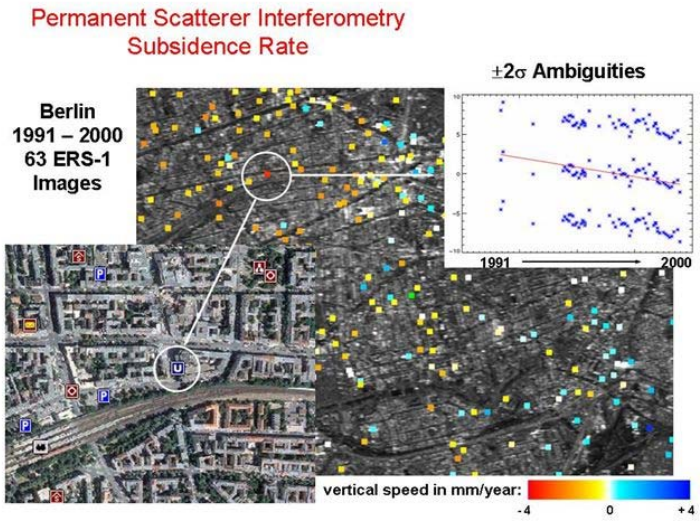

Fig. 17 Subsidence rate derived by the PS method. The marked point is a subway station and settles at a velocity of 2.5 mm/year compared to its neighbourhood. 63 ERS data sets from 1991 to 2000 have been used. The plot shows the relatively low noise of the measurement. The ± 2ð ambiguities areplotted for easier interpretation.

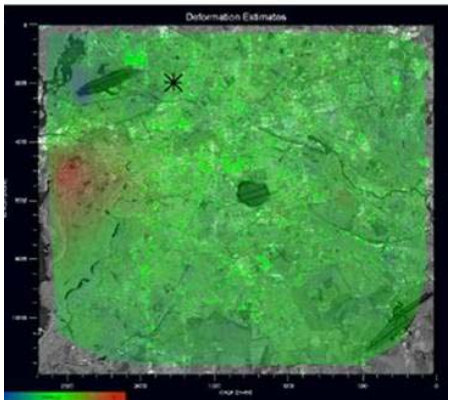

Fig.18 Inflation due to ground water regulation at the Berlin Olympic stadium. PS measurements have been spatially interpolated to allow for a better visual interpretation; green: no subsidence / inflation, red: inflation of 4 mm/year, cross: reference point, assumed to be stable: (Kampes et al., 2003).

8. Multifrequency SAR Interferometry

A multi-frequency SAR system offers a great potential to improve the unwrapping performance of Interferogrammes.

The SIR-C/X-SAR Shuttle Mission flown twice in April and October 1994 provided for the first time two pass interferometric data in X-, C-, and L-band gained simultaneously over some test areas. Respective investigations have shown that the availability of multi frequency information permits a drastic improvement of the phase unwrapping performance investigation [Moreira J. et. al 1995]. In the Fig 19 to 21 the sets of tree co-registered slant range images, coherence images, and a set of slant range interferometric phases overlapped with the interferometric magnitude images in L-, C-, and X-Band is depicted.

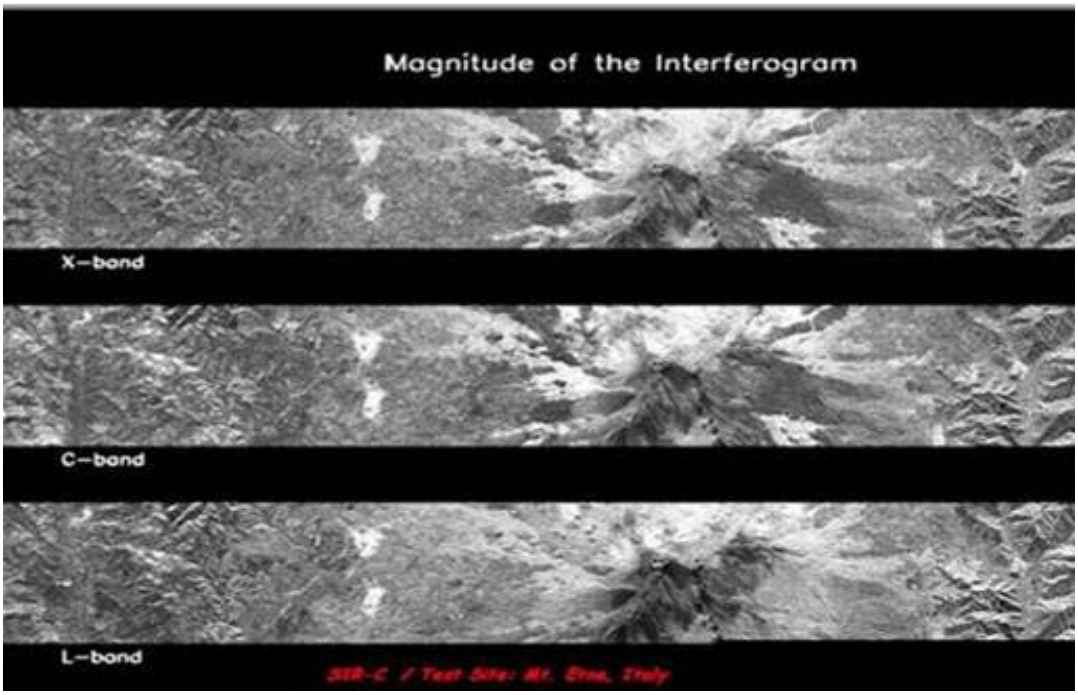

Fig.19 Set of co-registered slant range SAR images in L-, C-, and X-band. The image size is 66.8 km in azimuth and 9 km in ground range (16000 radar pulses and 1024 range bins in X-band and 2048 range bins in L- and C-band).

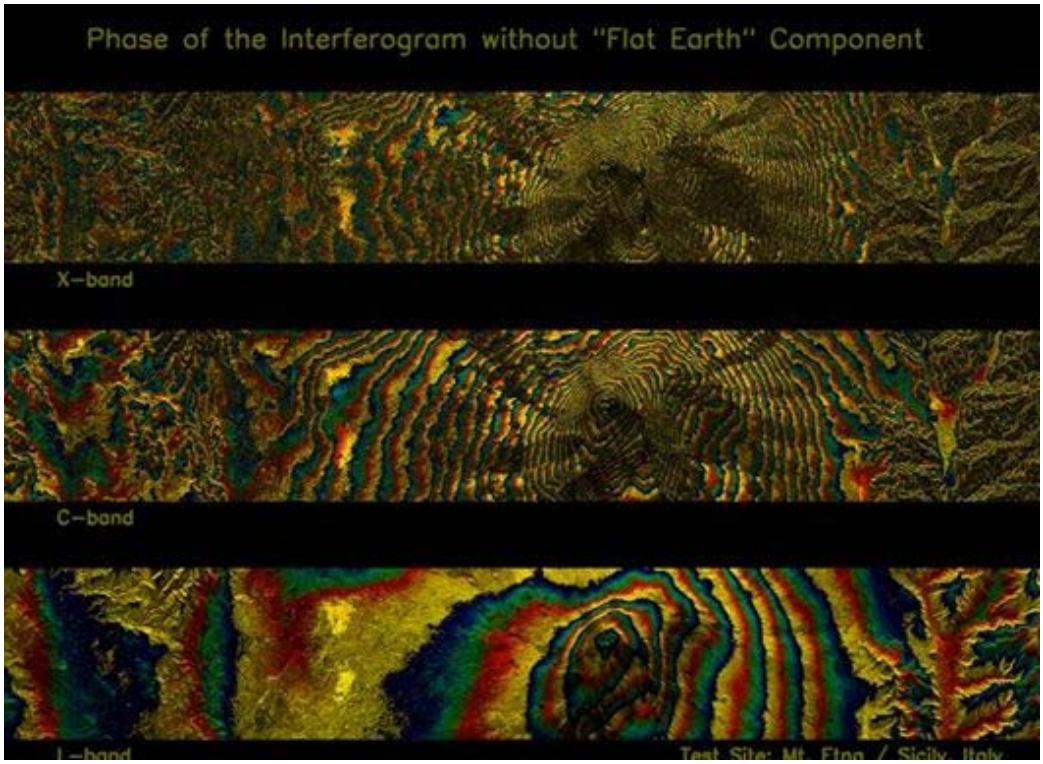

Fig.20 Set of co-registered interferometric Phase fringes in L-, C-, and X-Band overlapped with the respective magnitude images shown in Fig.18.

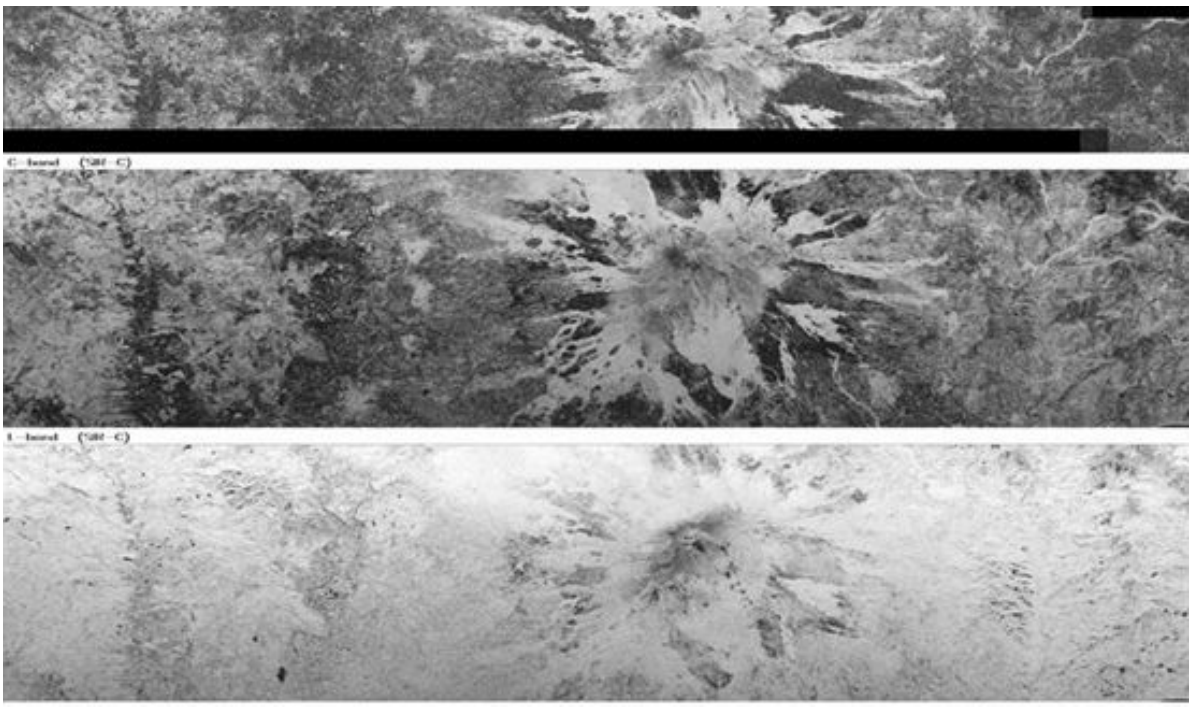

Fig.21 Set of co-registered slant range coherence images in L-, C-, and X-band. White indicates highcoherence and black low coherence. It is evident that l-Band has a high coherence with the exception of certain small areas

Considering an image pair which meets the baseline and Doppler centroid requirements, the interferometric phase quality is limited by the temporal de-correlation as has been mentioned already. The height accuracy depends on both the wavelength and the coherence. For areas with the same coherence for L-, C-, and X-band, the height derived from the X-band phase is approximately two times more accurate than C-band and eight times more than L-band due to the wavelength ratios.

In the example of SIR-C/X-SAR, the basic shape of the fused DEM, i.e. the low frequency part, is mainly derived from L-band due to its high coherence. The high frequency part of the DEM is derived from C- and X-band due to their small wavelengths. This fusion is done by using a simple Kalman filter and takes into account the respective coherences.

The phase gradient estimation can be improved drastically in the presence of critical areas, i.e. low-coherence areas, if an a priori knowledge of the terrain topography is available. The main idea is to improve the unwrapping procedure in C- and X-band by using, as a priori information, the L-band unwrapped values. The selection of the L-band data is related to its higher coherence and the lower sensitivity, compared to C- and X-band data, of the interferometric phase to the variations of the height profile.

A block diagram of the multi frequency unwrapping procedure is depicted in Fig 22. The first step of the proposed procedure is represented by the filtering operation of the L-band wrapped phase (via a 3 x 3 pixel pivoting median filter) followed by the phase unwrapping step. The L-band unwrapped data are used to improve the C-and X-band unwrapping results following the procedure depicted in Fig.22.

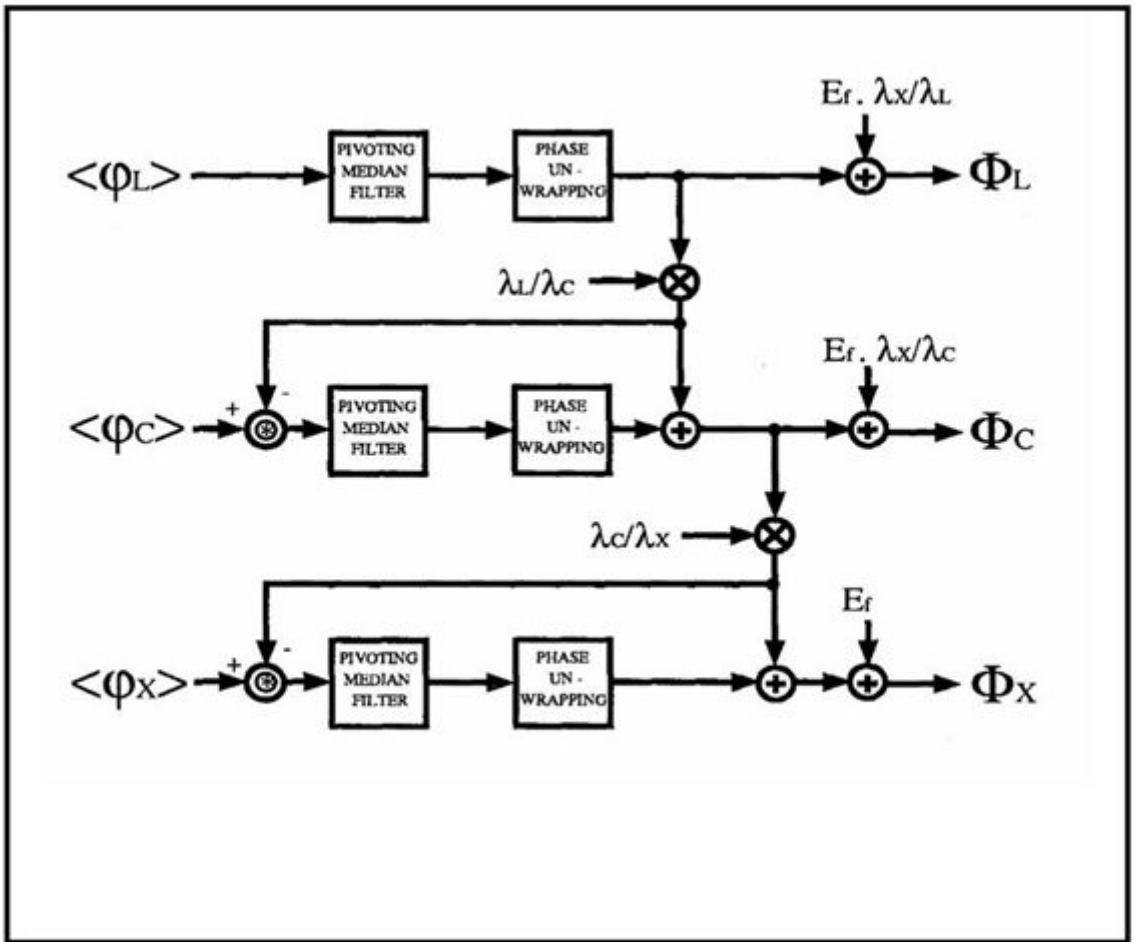

Fig.22 Block diagram of the multi-frequency phase unwrapping procedure. (<φL >, (<φC > and < φX > are the wrapped phases of the L-, C-, and X-band, respectively, without the flat-earth component; .λ_L, λ_C, λ_X are the wavelengths. E_f is the flat-earth function scaled for X-band also used in the L- and C-band with the respective wavelength scaling. * denotes the phase difference calculated in the complex domain. Φ_L, Φ_C,Φ_X are the unwrapped original phases in the respective Bands.

First of all, the resulting L-band phase is scaled with respect to the C-band wavelength and subtracted from the C-band measured phase. This operation is carried out in the complex domain so that:

- both rescaled L-band and C-band phases are transformed into complex signals by using an unitary amplitude,
- the difference operation is realized by multiplying the complex C-band signal by the complex conjugate of the L-band signal, and
- the wrapped phase difference is obtained from the arctangent of the above-mentioned complex multiplication

The result of the difference operation is filtered with a 3 x 3 pivoting median filter and then unwrapped. It should be noted explicitly that the pivoting median filter will benefit from the improved phase field stationary due to the performed subtraction. Finally, the computed phase is added to the L-band reference signal.

The same strategy is used to unwrap the X-band phase Interferogramme. The only difference in this case is that the previously computed C-band phase, instead of the L-band one, is used as a reference pattern. The overall procedure block diagram is depicted in Fig. 23.

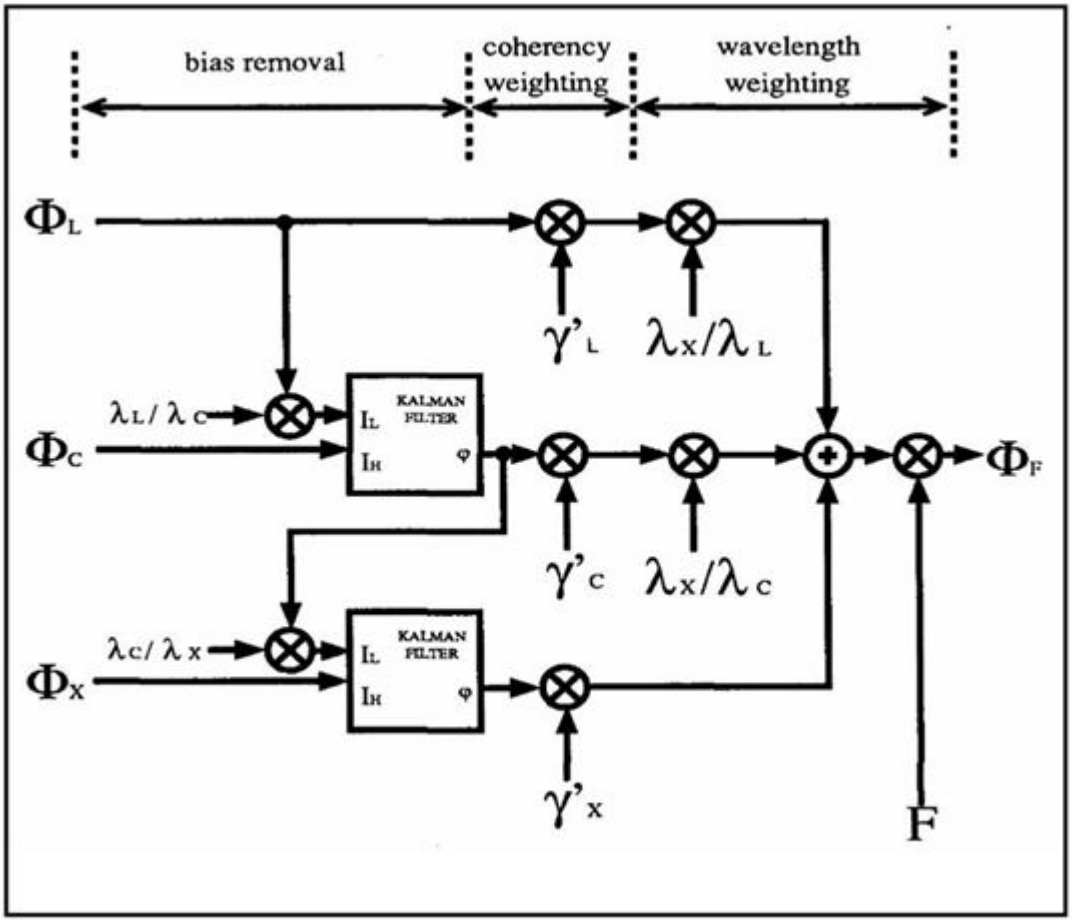

Fig. 23 Block-diagram of the Phase Fusion Algorithm

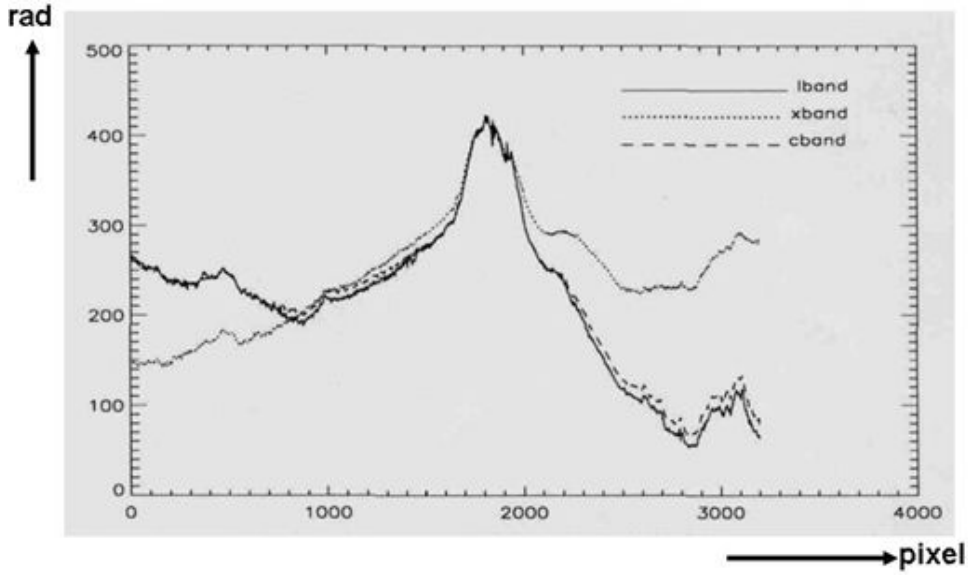

Fig. 24 Unwrapped phase profiles(azimuth direction) filtering without unwrapped phase profiles of L-, C-, and X-band in azimuth direction applying multi-frequency phase unwrapping without filter before phase unwrapping. The L- and C-band phases were scaled with respect to the X-band wavelength for comparison purposes. The x-axis gives the azimuth dimension in pixels. Each pixel has a size of 20.9 m (3200 pixels correspond 66.864 km). The y-axis unit is radians.

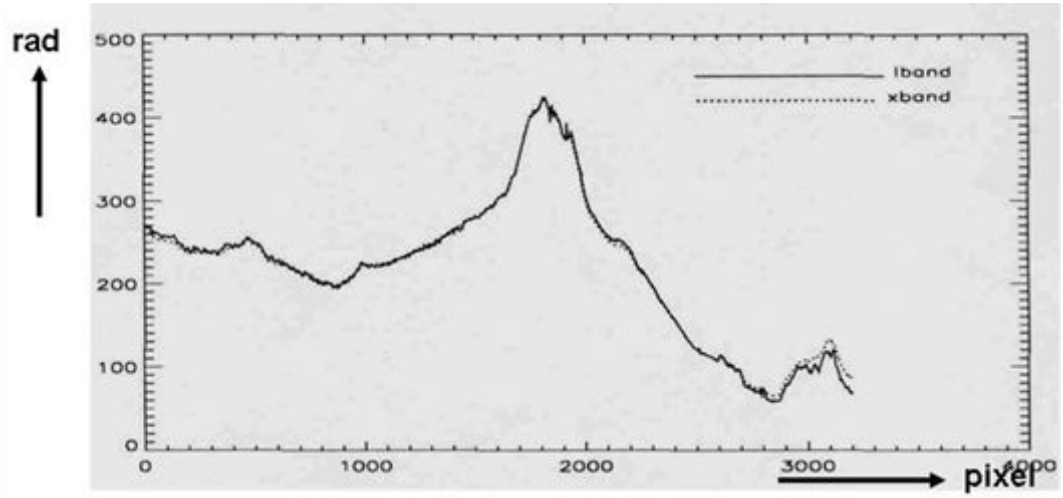

Fig. 25 Unwrapped phase of L-, and X-band profiles in azimuth direction applying multi-frequency phase unwrapping with the cascade of two filters with a window of 5x5 before phase unwrapping. The L- phase was scaled with respect to the X-band wavelength for comparison purposes. The x-axis gives the azimuth dimension in pixels. Each pixel has a size of 20.9 m (3200 pixels correspond 66.864 km). The y-axis unit is radians.

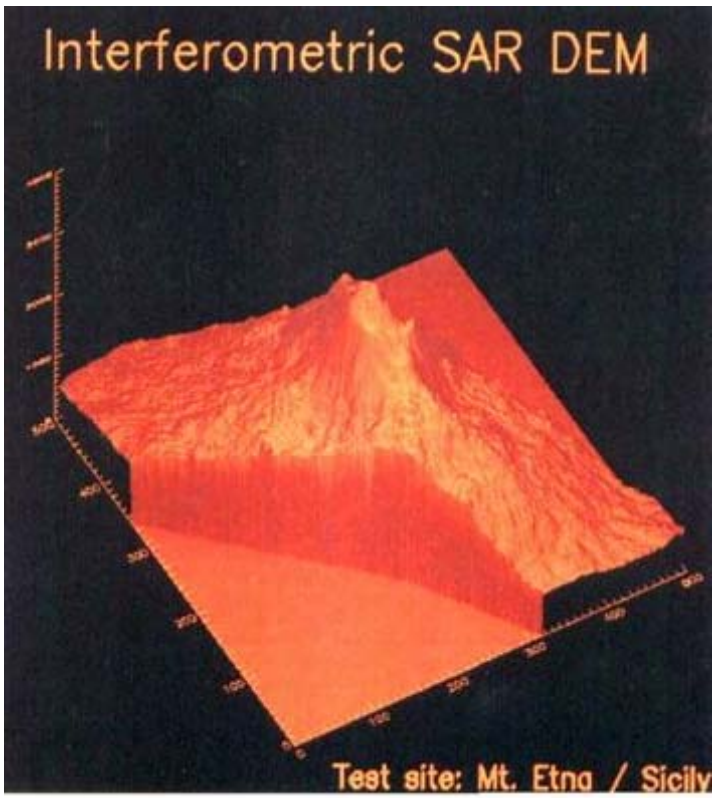

Fig 26 Perspective view of the geo-coded DEM of the Mount Etna area. The size of the x-y plane is 25 km x 25 km, the unit along the z-axis is meters.

To demonstrate the improvement achieved by using the multi-frequency information the corresponding results obtained by independently unwrapping the three Interferogrammes without any filtering and filtered are depicted in Fig.24 and Fig. 25 which show slices through an unwrapped Interferogamme before and after filtering (next page). The comparison makes evident the joint effects of the filtering step combined with the introduction of the multi-frequency information. In Fig. 24 there are still some reconstruction problems caused by extremely low-coherence areas present in the X-band data where the bias could not be completely avoided. A better result can be obtained by applying stronger data filtering. This is shown in Fig. 25, where the L-band reference is compared to a highly filtered X-band unwrapped pattern (retrieved in the multi-

frequency phase unwrapping procedure by using the cascade of two 5x5 median filters). Obviously, the improvement obtained is at the expense of a loss in the height resolution in X-band. In Fig. 26 is the resulting DEM of the Mount Etna depicted.

9. SAR Tomography

Interferometry determines by means of the phase differences between two different sensor positions the terrain topography. Although it is possible in this way to find a three-dimensional (3-D) surface representation, the distribution of the different scatterers in the height direction at a fixed range and azimuth position remains unknown. Contrary to this, tomographic techniques enable a real geometric resolution capability in the height direction and introduce new possibilities for many applications and inversion problems. Even misinterpretations in SAR images caused by layover and foreshortening effects can be solved by the tomographic processing.

The combination of interferometric and polarimetric techniques enables the separation of different scattering mechanisms within a resolution cell and at the same time, the estimation of the associated heights. The phase decomposition performed in polarimetric SAR interferometry uses the full polarimetric data and estimates for each image pixel three orthogonal scattering mechanisms. For example, for a vegetated area the three different scattering mechanisms can be described as (in a simplified model):

1) a single bounce contribution from the ground;

2) a double bounce contribution from the trunks; and

3) a diffuse (volume) contribution from the tree leaves and branches.

However, it is not possible with this technique to separate the contributions of the same scattering mechanism distributed over different heights.

The basic idea of Tomography is to form a second synthetic aperture in the direction of the translational movement (see Fig. 27). This direction, denoted as normal direction n, is perpendicular to the line-of-sight (range or across-track) **R** and azimuth (flight) directions **x**.

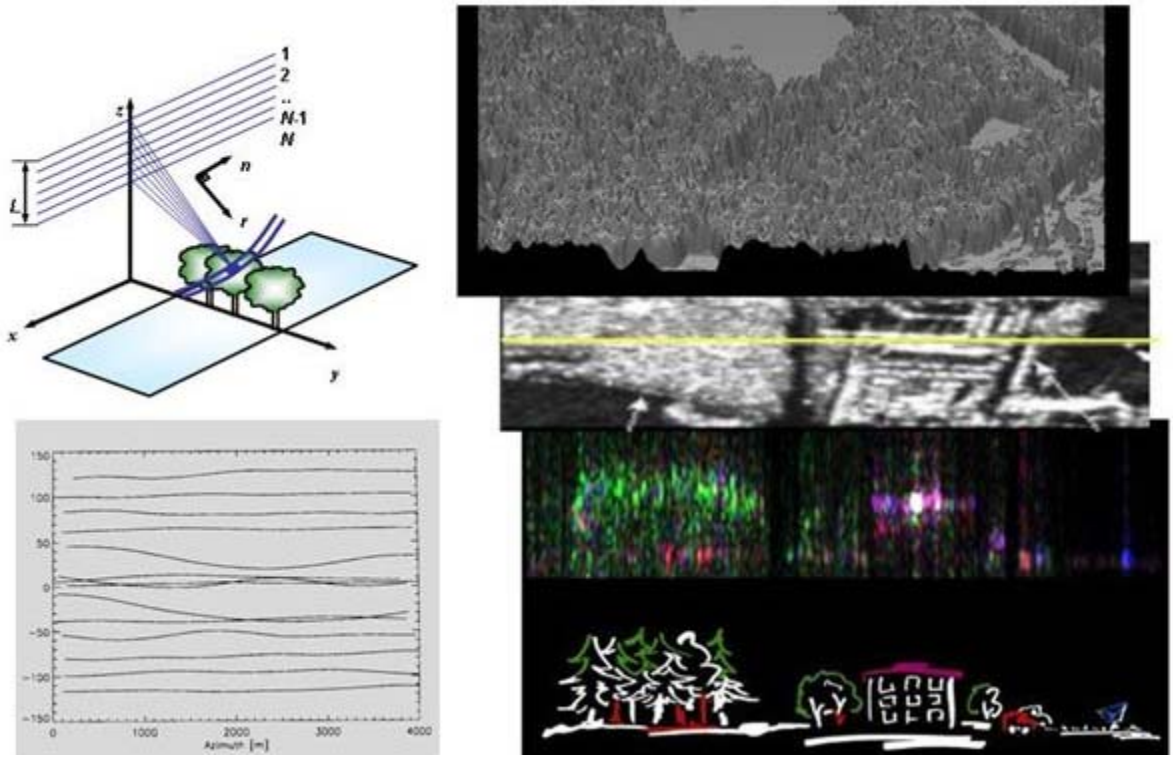

Fig. 27 Tomography for Scattering Analysis (Reigber, A., 1999) Left Part: Top Principle of SAR Tomography with Multiple horizontal Flights as Interferometry with Several Vertical Baselines, below real flight passes of a Do-228. Right part: E-SAR results. Top: 3-dim forest. Middle SAR image, yellow line indicates the flight path. Below: Colour coded different scattering mechanisms are obtained with polarization.The buildings roof is bright, the blue single bounce is the corner reflector, red double bounces happen at parts of the buildings roof and at the lower parts of trunks, in tree crowns and under story volume green scattering diffuse crosspol scattering dominates. Very below is artistic view of the imaged area.

The synthetic aperture in azimuth direction is associated with a variation of the so-called squint angle, while the synthetic aperture in the normal direction is associated with a variation of the off-nadir angle for each object.. Therefore, Tomograhy can be interpreted also as a multi baseline Interferometry with the number of tracks being much greater than two.

Remarkable is the deviation of the real flight passes in Fig. 27 from ideal strait lines. In connection with the former considerations on the influence of geometrical errors in Interferometry arrangements depicted in Table 3 for example this points out that motion compensation procedures are indispensable for exact interfeometric measurements. This will be discussed in the Systems Chapter again.

10. SAR Transponder Techniques for Absolute Altitude Calibration

Calibration for interferometric SAR systems is a conditio sine qua non as it is for all other SAR SAR sytems. Mainly, in that context the calibration of the amplitude of SAR signals is considered. An absolute altitude calibration in interferometric SAR can be performed via Transponder Techniques. The use of both active and passive transponder for SAR Calibration is a common and well developed techniqueThis will be discussed in more detail in the Systems chapter. But the absolute height calibration is more difficult than it seems under a first look.

In spite of the high resolution achieved by SAR, the resolving power is often insufficient to detect, identify and classify small objects in hard clutter environment. In such environments transponders with special coding can be used to identify objects in SAR images via tagging. The transponder modulates the signal received from the satellite with a characteristic code in range as well as in azimuth [Hounam. D, 1996] using signal modulation techniques, which affect the SAR signal in both range and azimuth and decouple the transponder signal from the background signal. This causes the transponder signal to be defocused and strongly suppressed in the SAR image. With a separate processing the transponder and the object on which it is mounted can thus be detected, located and identified even when situated in a high clutter area. Each trans-

ponder can be given an individual code. In principle, the transponder can be very small and lightweight. This offers advantages for both radiometric and three-dimensional geometric calibration. The retransmitted signal can be coded with respect to the transponder's three-dimensional exact position. This allows an exact determination of its three dimensional position especially of its absolute altitude also. (If the transponder is equipped additionally with a GPS receiver chip the GPS information can be inserted in the signal transmitted to the SAR also which would allow an unattended position determination). [Hounam, D. et. al., 1998, Bloetscher, H. et.al. 1998].

In the upper part of Fig 28 a Transponder signal within a highly cluttered ERS-1 scene is depicted in both situations before (left) and after (right) decoupling of the signal from the imaged background. The strong suppression of the transponder in the SAR Image is evident as well as the strong evidence of the Transponder signal after Processing which takes into account the special Transponder code. The upper images are the three dimensional SAR signals of the ERS-1, the lower image is a conventional SAR imge of the same scene. The small white circle in the middle of the lower images gives the Position of the Transponder.

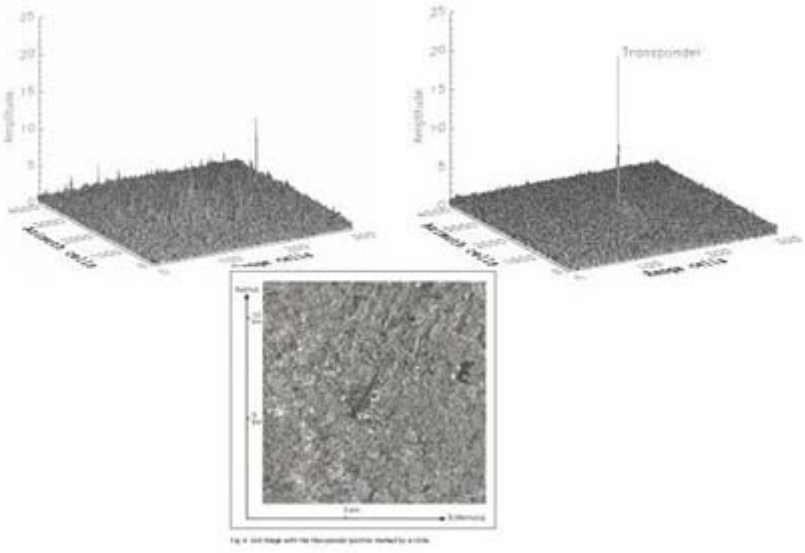

Fig. 28 Really measured example of a coded Transponder in a clutter surrounding of an ERS-1 scene. Upper left and lower image: the Trans-ponder is shadowed completely and not detectable. Upper right image: The Transponder clearly shows up after a specially converted processing.

11. References

Books

Curlander, J. C., R. N. McDonough. *Synthetic Aperture Radar Systems and Signal Processing*. Wiley Series in Remote Sensing. John Wiley & Sons [1991].

Franceschetti, G., R. Lanari. Synthetic Aperture Radar Processing. CRC Press [1999].

Ghiglia, D. C., M. D. Pritt. *Two-dimensional Phase Unwrapping,Theory, Algorithms, and Software*. JohnWiley & Sons [1998].

Hanssen, R. 2001, Radar Interferometry: Data Interpretation and Error Analysis, Kluwer Academic Publishers, Dordrecht, The Netherlands.

Henderson F.M., A.l. Lewis (Editors): Principles and Applications of Imaging Radar, John Wiley and Sons, Inc.1998

Scheiber, R.: High Resolution Interferometry for Synthetic Aperture Radar (in German), Doctoral Thesis University of Karlsruhe (TH), DLR-Forschungsbericht 2004-12, 2004

Articles and Presentations

Adama N., B. Kampesa, M. Einedera,J. Worawattanamateekulb. M. Kircherb The Development of a Scientific Permanent Scatterer System DLR ,2003

Adam N . B. Kampes, "Permanent Scatterer: Software Documentation",DLR-IMF internal TNs, 2002

Atteraa, E.P.W., 1991. The Active Microwave Instrument Onboard the ERS-1 Satellite, Proc. of the IEEE, Vol. 79, No. 6, pp. 791-799

Bamler, R: SAR-Interferometry, Lecture at Munich Summer school, "Munich Research Association for Remote Sensing of the Environement",MFFU, Ludwig-Maximilians-University Munich 2000

Bloetscher, H., D.Geudtner, D.Hounam, K.Waegel, M. Zink, „A new concept of Radiometric, Polarimetric and Interferometric SAR calibration",Proc. EUSAR'98,Friedrichshafen, May 1998, pp. 209- 212.

Breit, M. Eineder H., J. Holzner, H. Runge, R. Bamler Traffic Monitoring using SRTM Along-Track Interferometry, Proc. IEEE IGARSS July 21-25, 2003 Toulouse, France

Bamler R.M.Eineder, B.Kampes, H.Runge, n.Adam, SRTM and Beyond: Current Situation and new developments in space-borne InSAR

Bamler, R.,. Geudtner, B. Schättler, P. Vachon, U. Steinbrecher, J. Holzner, J. Mittermayer, H. Breit, A. Moreira. RADARSAT ScanSAR interferometry. In: Proc.IGARSS'99, pp. 1517 - 1521. Hamburg [1999].

Bamler, R.,. Hartl. Synthetic aperture radar interferometry. Inverse Problems, 14, pp. R1-R54 [1998].

Bao, M., J. Schulz-Stellen_eth, S. Lehner, M. Eineder. First results on ocean wave imaging from the shuttle radar topography mission (SRTM). In: Proceedings of IGARSS'01, pp. 584ñ586. Sydney [2001].

Bara, M., R. Scheiber, A. Broquetas, A. Moreira. Interferometric SAR signal analysis in the presence of squint. IEEE Trans. on Geoscience and Remote Sensing, 38, no. 5, pp. 2164ñ2178 [2000].

Bertiger, W.I., Y.E. Bar-Sever, E.J. Christensen, E.S. Davis, J.R. Guinn, B.J. Haines, R.W. Ibanez-Meier, J.R. Jee, S.M. Lichten, W.G. Melbourne, R.J. Muellerschoen, T.N. Munson, Y. Vigue, S.C. Wu, T.P. Yunck, B.E. Schutz, P.A.M. Abusali, H.J. Rim, M.M. Watkins, and P. Willis, 1995. GPS Precise Tracking of TOPEX/Poseidon: Results and Implications, J. .Geoph Res., Vol. 99, No. C-12, pp 24449-24464

Breit H., M. Eineder, J. Holzner, H. Runge, R. Bamler, Traffic Monitoring Using SRTM Along-Track Interferometry, Proc.IGARSS 2003, Toulouse, France,

Buckreuss S., J. R. Moreira, H. Rinkel and G. Waller. "Advanced SAR Interferometry Study". DLR Internal Report, MIT 94-10, June 1994.

Carande, R.E., 1994. Estimating Ocean Coherence Time Using Dual-baseline Interferometric Synthetic Aperture Radar, IEEE Trans. Geoscience and Remote Sensing, Vol.32, No.4, pp. 846-854

Carrara, W. G., R. S. Goodman, R. M. Majewski. Spotlight synthetic aperture radar: signal processing algorithms. Artech House [1995].

Cloude S. R., K. P. Papathanassiou, "Polarimetric SAR interferom-etry," IEEE Trans. Geosci. Remote Sensing, vol. 36, pp. 1551-1565, Sept. 1998.

Coltelli, M. et al: SIR-C/X-SAR Interferometry over Mt. Etna: DEM Generation, Accuracy Assessment and Data Interpretation. DLR-Forschungsbericht, FB 95-48, Feb. 1996

Carande, R.E., 1994. Estimating Ocean Coherence Time Using Dual-baseline Interferometric Synthetic Aperture Radar, IEEE Trans. Geoscience and Remote Sensing, Vol.32, No.4, pp. 846-854

Davidson, G. W., I. Cumming. Signal properties of space-borne squint-mode SAR. IEEE Trans. On Geoscience and Remote Sensing, 35, no. 3, pp. 611ñ617 [1997].

Dixon, T., Ed., 1995. SAR Interferometry and Surface Change Detection, Report of Workshop, Boulder, Feb. 3-4, 1994, University of Miami, RSMAS Technical Report TR 95-003, Published July 1995.

Eineder, M., R. Bamler, N. Adam, S. Suchandt, H. Breit, U. Steinbrecher, B. Rabus, W. Knˆp_e. Analysis of SRTM interferometric X-band data: First results. In: Proc.IGARSS'00, pp. 2593ñ2595. Hawaii [2000].

Eineder, M., 2003. Oscillator Clock Drift Compensation in Bistatic Interferometric SAR. In: Geoscience and Remote Sensing Symposium Proceedings, IEEE IGARSS, Toulouse, 2003.

Eineder M, S. Lehner: Discussion of TerraSAR-X Potential for Object Motion Measurements using Along Track Interferometry (ATI), Internal Technical Note TS-MF-POMMATI, 7.8.2002.

Ender, J. H. G.: "Detection and Estimation of MovingTarget Signals by Multi Channel SAR", in "EUSAR '96", Königswinter, Germany, 1996., VDE-Verlag, 1996, pp 411-417.

Evans, D.L., T.G. Farr, H.A. Zebker, J.J. van Zyl, and P.J. Mouginis-Mark, 1992. Radar Interferometry Studies of the Earth's Topography, Eos Trans. American Geophysical Union, Vol.73, No.52, pp. 553-558

Ferretti A., C.Prati F. ROCCA, "Analysis of Permanent Scatterers in SAR Interferometry", IEEE 2000,

Ferretti A., C. Prati, and F. Rocca, "Nonlinear Susidence RateEstimation usingPermanent Scatterer in differential SAR Interferometry," *IEEE Trans.GRSS*, vol. 38, no. 5, pp. 2202 -2212, 2000

Ferretti A., F. FERUCCI, C. PRATI AND F. ROCCA, "SAR Analysis of Building Collapse by means of the Permanent Scatterer Techniques", IEEE 2000"

Frasier, S. J., A. J. Camps. Dual-beam interferometry for ocean surface current vector mapping. IEEE Trans.on Geoscience and Remote Sensing, 39, no. 2, pp. 401-414 [2001].

Gatelli, F., A. M. Guarnieri, F. Parizzi, P. Pasquali, C. Prati, F. Rocca. The wavenumber shift in SAR interferometry. IEEE Trans. on Geoscience and Remote Sensing, 32, no. 4, pp. 855-865 [1994].

Gabriel, A.K. and R. M. Goldstein, 1988. Crossed Orbit Interferometry: Theory and Experimental Results from SIR-B, International Journal of Remote Sensing, Vol. 9, No. 5, pp. 857-872

Gabriel, A.K. et al: Mapping Small Elevation Changes Over Large Areas: Differential Radar Interferometry. J. Geophysical Research, Vol. 94, 1989, S. 9183-9191.Gatelli, P.,A. Monti Guarnieri, F. Parizzi, P. Pasquali, C. Prati, and F. Rocca, 1994. The Wavenumber Shift in SAR Interferometry, IEEE Trans. Geoscience and Remote Sensing, Vol. 32, No. 4, pp 855-865

Geudtner, D.; "The interferometric processing of ERS-1 SAR data"; European Space Agency, Technical Translation of DLR-FB 95-28, ESA-TT-1341, 1995.

Ghiglia, D.C , L.A. Romero. Robust Two-Dimensional Weighted and Unweighted Phase Unwrapping That Uses Fast Transforms and Iterative Methods. In: J. Opt. Soc. Am., vol. 11, 1994, S. 107-117

Gill, E., Runge, H., 2003. Tight Formation Flying for an Along-Track SAR Interferometer. In: Proceedings Space Generation Congress, IAC Bremen.

Goldstein, R. M., T.P. Barnett, and H.A. Zebker, 1989. Remote Sensing of Ocean Currents, Science, Vol. 246, pp. 1282-1285Goldstein, R. M., H. Engelhardt, B. Kamb, and R.M. Frolich, 1993. Satellite Radar Interferometry for Monitoring Ice Sheet Motion: Application to an Antarctic Ice Stream, Science, Vol. 262, pp. 1525-1530

Goldstein, R. M. et al: Satellite Radar Interferometry: Two-dimensional Phase Unwrapping. Radio Science, Vol. 5,1988, S. 416-425

Goldstein, R. M., C. L. Werner. Radar interferogram Filtering for geophysical applications. Geophysical Research Letters, 25, no. 21, pp. 4035-4038 [1998].

Goldstein, R. M., Zebker, H.A.: Interferometric Radar Measurement of Ocean Surface Current. In: Nature, Vol. 328,1987, S. 707-709.

Graham, L.C.,1974.Synthetic Interferometer Radar for Topographic Mapping, Proc. IEEE, Vol. 62, pp. 763

Gray A.L. and P.J. Farris-Manning, 1993. Repeat-pass Interferometry With Airborne Synthetic Aperture Radar, IEEE Trans. Geoscience and Remote Sensing, Vol. 31, No. l, pp. 180-191

Griffin, M.F., E.G. Boman, I. Metal, and L. Orwig, 1993. Estimating Ocean-scene Coherency-time With a Multi-aperture Radar, IEEE Int. Conf. of Acoustics, Speech, and Signal Processing, ICASSP-93, Vol. 5, pp. 461-464

Greidanus, H., E. Huising, Y. Platschorre, R. V. Bree, D. V. Halsema, E. Vaessen. Coastal currents withalong-track interferometry. In: Proceedings of IGARSS'99, pp. 2607-2609. Hamburg [1999a].

Hartl, P. ,H.M. Braun: A Bistatic Parasitical Radar (BIPAR), In: Proc.ISPRS Symp., Kyoto, Japan, 1988.

Hellwich O., A. Reigber, S. Guillaso, M. Jaeger, M. Neumann, A. Bellmann: "Current Developments in Airborne SAR Remote Sensing",Photogrammetric Week '05, 2005

Hirsch, O. Neue Verarbeitungsverfahren von Along-Track Interferometrie Daten eines Radars mit synthetischer Apertur [2002]. Submitted as PhD thesis, Universität Siegen, Germany.

Holzner, J., Bamler, R., 2002. Burst-Mode and ScanSAR Interferometry. IEEE Transactions on Geoscience and Remote Sensing, vol. 40, no. 9, pp. 1917-1934.

Hounam, D. „Ortung von eindeutig identifizierbare Zielen in SAR-Bildern mit kodierten Transpondern", Dissertation Uni. Stuttgart, Inst. für Navigation 1996

Hounam, D., K.Waegel, „Method and Device for Locating and Identifying Objects by Means of an encoded Transponder,"U.S patent Nr.5,821,895, October 1998

D. Hounam, „Ortung von eindeutig identifizierbaren Zielen in SAR Bildern mit kodierten Transpondern", Thesis Nr. 482, Reihe C,1998, Verlag der Bayerischen Akademie der Wissenschaften, Muenchen

Jin, M. Y., C. Wu. A SAR correlation algorithm which accomodates large range migration. IEEE Trans. On Geoscience and Remote Sensing, 22, pp. 592-597 [1984].Jordan, R.L., 1980, The SEASAT-A Synthetic Aperture Radar System, IEEE Jour, of Oceanic Engineering, Vol. OE-5, No. 2, pp. 154-164

Just, D., R. Bamler. Phase statistics of interferograms with applications to synthetic aperture radar. Applied Optics, 33, no. 20, pp. 4361- 4368 [1994].

Kampes, B.M., Adam, N., 2003. Velocity field retrieval from long-term coherent points in radar interferometric stacks. In: Geoscience and Remote Sensing Symposium Proc., IGARSS, Toulouse, 2003.

Keydel, W., Hounam D., Pac R., Werner M. (2000):X-SAR/SRTM - Part of a global Earth Mapping Mission. RTO Meeting Proceedings 61, Space-Based Observation Technology, RTO MP-61, ISBN 92-837-1050-9, October 2000, p. 32 ff

Kircher, M., A. Roth, N.Adam, B. Kampes, H. J. Neugebauer, Remote Sensing Observation of Mining Induced Subsidence by means of differential SAR-Interferometry , IGARSS 2003,

Koch, A., Heipke, C., Lohmann, P., 2002. Analysis of SRTM DTM — Methodology and practical results. The International Archives of the Photogrammetry Remote Sensing and Spatial Information Sciences, Com. IV, Ottawa, Vol. XXXIV, part 4, pp. 470-475

Krieger, G., Wendler, M., Fiedler, H., Mittermayer, J., Moreira, A., 2002. Performance analysis for bistatic interferometric SAR configurations. In: Proc.IGARSS 2002, Toronto, Canada, vol. 1, pp. 650-652.

Krieger, G., Fiedler, H., Mittermayer, J., Papathanassiou, K., Moreira, A.: "Analysis of Multi-Static Configurations for Spaceborne SAR Interferometry," IEE Proc. for Radar, Sonar and Navigation, 2003.

Lang, O., Rabus, B., Dech, S.W., 2003. Velocity Map of the Thwaites Glacier Catchment, West Antarctica. Submitted to: Journal ofGlacioIogy.

Lee, J.-S., K. W. Hoppel, S. A. Mango, A. R. Miller. Intensity and phase statistics of multilook polarimetric and interferometric SAR imagery. IEEE Trans. GRSS, 32, pp. 1017 -1028 [1994].

Klimach, H. W., and G. T. Sos, 1994. High Performance Interferometric SAR Description and Capabilities, Proceedings of First International Airborne Remote Sensing Conference and Exhibition, September 11-15, Strasbourg, France, Vol. 3, pp. 697-710

Krieger, G., Fiedler, H., Mittermayer, J., Papathanassiou, K., Moreira, A.: "Analysis of Multi-Static Configurations for Spaceborne SAR Interferometry," IEE Proc. for Radar, Sonar and Navigation, 2003.

R. Lanari, G. Fornaro, D. Riccio, M. Migliaccio, K. Papathanassiou, J. R. Moreira, M. Schwabisch, L Dutra, G. Puglisi, G. Franceschette, M. Coltelli, "Generation of Digital Elevation Models by Using SIR-C/X-SAR Multi-Frequency Two-Pass Interferometry: the Etna Case Study". IEEE Trans. on Geosc. and Remote Sensing, Sept. 1996

Li, F. and R. M. Goldstein, 1990. Studies of Multi-baseline Spaceborne Interferometric Synthetic Aperture Radars, IEEE Trans. Geoscience and Remote Sensing, Vol. 28, No. 1, pp. 88-97

Madsen, S.N., H.A. Zebker and J.M. Martin, 1993. Topographic Mapping Using Radar Interferometry: Processing Techniques, IEEE Trans. Geoscience and Remote Sensing, Vol. 31, No. 1, pp 246-256

Madsen, S.N., J.M. Martin and H.A. Zebker, 1995. Analysis and Evaluation of the NASA/JPL TOPSAR Across-track Interferometric SAR System, IEEE Trans. GRSS., Vol. 33, No. 2, pp. 383-391.

Madsen, S.N., 1995. On Absolute Phase Determination Techniques In SAR Interferometry, SPIE Conference on Radar Sensor Technology, SPIE-2487, April, pp. 393-401.

Marom, M., R.M. Goldstein, E.B. Thornton, and L. Shemer, 1990. Remote Sensing of Ocean Wave Spectra by Interferometric Synthetic Aperture Radar, Nature, Vol. 345, pp. 793-795

Massonnet, D. 1999: Capabilities And Limitations of the Interferometric Cartwheel, Proceedings of the CEOS Workshop, Oct. 1999. Manuscript available at http://www.estec.esa.nl/confannoun/99b02/index.html

Massonnet, D., K. Feigi, M. Rossi, and F. Adragna, 1994. Radar Interferometric Mapping of Deformation in the Year After the Landers Earthquake, Nature, Vol. 369, pp. 227-230

Massonnet, D., M. Rossi, C. Carmona, F. Adragna, G. Peltzer, K. Feigi, and T. Rabaute, 1993. The Displacement Field of the Landers Earthquake Mapped by Radar Interferometry, Nature, Vol. 364, 138-142

Massonnet D., E. Thouvenot, S. Ramongassie, L. Phalippou, A wheel of passive radar microsats for upgrading existing SAR projects, IEEE IGARSS, 2000

Mittermayer, J., G. Krieger, M. Wendler, A. Moreira, E. Thouvenot, T. Amoit, R. Bamler. Interferometric performance estimation for the interferometric Cartwheel in combination with a transmitting SAR satellite.Proceedings of IGARSS'2001, pp. 2955-2957. Sydney [2001].

Mittermayer J., A. Moreira, and O. Loffeld, "The frequency scaling algorithm for spotlight SAR data processing," IEEE Trans. Geosci. Remote Sensing, vol. 37, Sept. 1999.

Moore, R. K., J. P. Claassen, Y. H. Lin. Scanning space-borne synthetic aperture radar with integrated radiometer. IEEE Trans. on Aerospace and Electronic Systems, 17, pp. 410-420 [1981].

Moreira A., J. Mittermayer, and R. Scheiber, "Extended chirp scaling algorithm for air- and spaceborne SAR data processing in stripmap and ScanSAR imaging modes," IEEE Trans. Geosci. Remote Sensing, vol. 34, pp. 1123-1136, Sept. 1996

Moreira, A., G. Krieger, J. Mittermayer. Comparison of several bi-static SAR configurations for space borne SAR interferometry [2001]. Oral presentation at IGARSS'01 symposium, Sydney.

Moreira, J. Bewegungsextraktionsverfahren für Radar mit synthetischer Apertur . DLR technical report FB92-31, Technische Universität München [1992].

Moreira , J. R. and W. Keydel, "A new MTI –SAR approach using the reflectivity displacement method", IEEE Transactions on Geoscience and Remote Sensing., vol. 33, no. 5, pp. 1238-1244, 1995.

Moreira J., M. Schwäbisch, G. Fornaro, R. Lanari, R. Bamler, D. Just, U. Stein-brecher, H. Breit, M. Eineder, G. Franceschetti, D. Geudtner, H. Rinkel, "X-SAR In-terferometry: First Results", IEEE Transactions on Geosc. and Remote Sens., vol. 33, No. 4, pp. 950-956, July 1995.

N.N.;Coastal, DEMs with cross-track interferometry. In: Proceedings of IGARSS'99, pp. 2161-2163. Hamburg[1999b].Nemoto, Y., H. Nishino, M. Ono, H. Mizutamari, K. Nishikawa, and K. Tanaka, 1991. Japanese Earth Resources Satellite-1 Synthetic Aperture Radar, Proc. IEEE, Vol.79, No.6, pp 800-809

O'Brien, J.D., H. Pullman, H. Holt Jr., and L. Orwig, 1994. Accuracy Validation of the IFSARE Radar System, Natl. Aerospace and Electronics Conference, NAECON 94, Vol. 1, pp. 234-238

Papathanassiou K. P., "Polarimetric SAR interferometry," Ph.D. dissertation. Uni. Tech., Graz, Austria, 1999

Peltzer, G. and P. Rosen, 1995. Surface Deformation Associated with the May 17, 1993 Eureka Valley, California Earthquake Observed by SAR Interferometry, Science, Vol. 268, pp. 1333-1336.

Prats P, J.J. Mallorqui: "Estimation of azimuth phase undulations with multisquint processing in airborne interferometric SAR Images",IEEE TGRSLetter s, in press.

Prats P., J.J. Mallorqui, and A. Broquetas: “Calibration of interferometric airborne SAR images using a multisquint processing approach”, Proc. Of IGARSS’03, Toulouse, 2003.

Prats, P., A. Reigber and J.J. Mallorqui: “Topography Accommodation During Motion Compensation in Interferometric Repeat-pass SAR Images”,Proceedings of IGARSS’05, Seoul, Korea, July 2005

Prats P., A. Reigber and J.J. Mallorqui: “Retrieval of High-quality Interferometric SAR Products with Airborne Repeat-pass Systems”,Proceedings of IGARSS’05, Seoul, Korea, July 2005

Rabus B., M. Eineder, A. Roth, R. Bamler, The shuttle radar topography mission – a new class of digital elevation models acquired by spaceborne radar, ISPRS Journal of Photogrammetry and Remote Sensing, 57, pp. 241-262, 2003

Ramongassié S., L. Phalippou, E. Thouvenot, D. Massonnet, Preliminary Design of the Payload for the Interferometric Cartwheel, IEEE IGARSS, 2000

Raney, R. K., H. Runge, R. Bamler, I. G. Cumming, F. H. Wong. Precision SAR processing using chirp scaling. IEEE Trans. on Geoscience and Remote Sensing, 32, no. 4, pp. 786-799 [1994].

Reighber, A., SAR-Interferometry-An Introduction, Presentation made for the TMR SAR interferometry workshop held in Rennes/France 03.-07. April 2001, available at http://epsilon.nought.de

Reigber A. and R. Scheiber: “Differential SAR Interferometry Using an Airborne Platform”, Proceedings of EUSAR’02, K¨oln, pp. 373-376, 2002

Reighber, A., Moreira, A., Papathanasiou, K.: “First Demonstration of Airborne SAR Tomography using Multibaseline L-Band Data”. Proceedings of the IEE 1999 IGARSS’99, 28th June – 2nd July 1999, pp 44-46

Reigber A., P. Prats2,4, R. Scheiber3 and J.J. Mallorqui, Options for High-Precision Motion Compensation for Airborne Differential SAR Interferometry, 2003

Reigber A., P. Prats and J.J. Mallorqui: “Refined estimation of time-varying baseline errors in airborne SAR interferometry”, IEEE Geoscience and Remote Sensing Letters, Vol. 3, No. 1, pp. 145-149, January 2006

Reigber A., P. Prats and J.J. Mallorqui: “Refined estimation of time-varying baseline errors in airborne SAR interferometry”,Proceedings of IGARSS’05, Seoul, Korea, July 2005

Richman, D., 1982. Three-dimensionalAzimuth-correcting Mapping Radar, United States Patent 4321601.

Rodgers, A.E.E., and R.P. Ingalls, 1969. Venus: Mapping the Surface Reflectivity by Radar Interferometry, Science, No. 165, pp 797-799

Rodriguez, E., and J.M. Martin, 1992. Theory and Design of Interferometric Synthetic Aperture Radars, IEEE Proceedings-F, Vol. 139, No. 2, April 1992, pp. 147-159.

Rodriguez, E., D.Imel, and S.N. Madsen, 1995. The Accuracy of Airborne Interferometric SARs, IEEE Trans. Aerospace and Electronic Systems

Romeiser R., H. Breit, M. Eineder, H. Runge, P. Flament, K. de Jong, J.Vogelzang: Validation of SRTM-Derived Surface Currents Off The Durch Coast By Numerical Circulation Model Results, Proc. IGARSS 2003, Toulouse, France, 2003

Romeiser R, H. Breit, M. Eineder, H. Runge, P. Flament, K. de Jong, J., Vogelzang, On The Suitability Of TerraSAR-X Split Antenna Mode For Current Measurements By Along Track Interferometry, IGARSS 2003, Toulouse, France, (in these proceedings)

Romeiser, R., Runge, H., Breit, H., Eineder, M., Flament, P., 2003. Towards an Operational Spaceborne System for High-Resolution Current Measurements in Coastal Areas. Submitted to: OCEANS’ 03, San Diego

Romeiser R., H. Breit, M. Eineder, H. Runge, “Demonstration of current measurements from space by along-track SAR interferometry with SRTM data”, Proc. IGARSS 2002, Toronto

Rumsey, H.C., G.A. Morris, R.R. Green, and R.M. Goldstein, 1974. A Radar Brightness and Altitude Image of a Portion of Venus, Icarus, No. 23, pp. 1-7

Runge, M. Eineder, H. Breit, P. Flament, R. Romeiser, Measurement Of Tidal Current Fields With SRTM Along Track Interferometry, EGSAGU-EUG Meeting Nice, France, 6-11 April 2003

Scharroo, R. ERS-1 operational orbit determination. In: E. Wisse, M. C. Naeije, R. Scharroo (Eds.), Processing of ERS-1 and TOPEX/Poseidon Altimeter Measurements, number 93-11 in BCRS report. Netherlands Remote Sensing Board [1993].

Scheiber R.: "A three-step phase correction approach for airborne repeatpass interferometric SAR data", Proceedings of IGARSS'03, Toulouse, 2003

Scheiber, R., A. Moreira. Coregistration of interferometric SAR images using spectral diversity. IEEE Trans.on Geoscience and Remote Sensing, 38, no. 5, pp. 2179-2191 [2000].

Scheiber R., A. Reigber, A. Ulbricht, K. P. Papathanassiou, R. Horn, S. Buckreuss, and A. Moreira, "Overview of interferometric data acquisition and processing modes of the experimental airborne SAR system of DLR," in Proc. IGARSS'99, Hamburg, Germany, 1999, pp. 35-38.

Scheiber R. and P. Robert: "Origin and Correction of Phase Errors in Airborne Repeat-Pass SAR Interferometry", Proc. of IGARSS'01, pp. 3114-3116, Sydney, 2001

Schulz-Stellen, J., J. Horstmann, S. Lehner, W. Rosenthal. Sea surface imaging with an across-track interferometric synthetic aperture radar: The SINEWAVE experiment. IEEE Trans. on Geoscience and Remote Sensing, 39, no. 9, pp. 2017-2018 [2001].

Schwäbisch, M., D. Geudtner. Improvement of phase and coherence map quality using azimuth pre_ltering: Examples from ERS-1 and X-SAR. In: Proceedings of IGARSS'95, pp. 205ñ207. Firenze, Italy [1995].

Shnitkin, H., 1994. Joint STARS Phased Array Radar Antenna, IEEE Proc. of the Antennas and Propagation Symposium, Seattle, Vol. 2, pp. 856-859

Stevens, D.R., I.G. Gumming, and L. Ray, 1995. Options for Airborne Interferometric SAR motion Compensation, IEEE Trans. Geoscience and Remote Sensing, Vol. 33, No.2, pp. 409-420.

Topographic Science Working Group, 1988. Topographic Science Working Group Report to the Land Processes Branch, Earth Science and Applications Division, NASA Headquarters, Lunar and Planetary Institute, Houston, 64 pp.

Siegmund, R. Bestimmung von topographischen und hydrologischen Parametern im Wattenmeergebiet mittels SAR-Interferometrie [2002]. PhD thesis, Christian-Albrechts-Universität Kiel, Germany

Soumekh, M. Synthetic Aperture Radar Signal Processing. Wiley & Sons [1999].

Ulbricht A., "Flugzeuggetragenene repeat-pass interferometrie mit dem E-SAR," Ludwig-Maximilian Univ. Munchen, Munchen, Germany, 2000.

Zebker H.A, P.A. Rosen, R.M. Goldstein, A. Gabriel, and C. Werner: "On the derivation of coseismic displacement Fields using differential radar interferometry: the Landers earthquake," Journal of Geophysical Research, Vol. 99, pp. 19617-19634, 1994.

Zebker, H. and R. Goldstein, 1986. Topographic Mapping from Interferometric SAR Observations, Journal of Geophysical Research, Vol. 91, B5, pp. 4993-4999

Zebker, H.A., and J. Villasenor, 1992. Decorrelation in Interferometric Radar Echoes, IEEE Trans. Geoscience and Remote Sensing., 1992, Vol. 30, No. 5, pp. 950-959

Zebker, H.A., C. Werner, P.A. Rosen, and S. Hensley, 1994a. Accuracy of Topographic Maps Derived from ERS-1 Interferometric Radar, IEEE Trans. Geoscience and Remote Sensing, Vol. 32, No. 4, pp. 823-836.

Zebker, H.A., P.A. Rosen, R. M. Goldstein, C. Werner, and A. Gabriel, 1994b. On the Derivation of Coseismic Displacement Fields Using Differential Radar Interferometry, Journal of Geophysical Research-Solid Earth, Vol. 99, No. 10, pp. 19617-19634

Zebker, H.A., T.G. Farr, R. Salazar, and T. Dixon,1994c. Mapping the World's Topography with Radar Interferometry, Proceedings of the IEEE, Vol. 82, No. 12, pp. 1774-17